

Seton Hall University

eRepository @ Seton Hall

Seton Hall University Dissertations and Theses
(ETDs)

Seton Hall University Dissertations and Theses

Spring 5-18-2020

d-Orbital Occupancy of Transition Metal Oxides by X-Ray Absorption Near Edge Structure (XANES)

Eric Kurywczak

eric.kurywczak@student.shu.edu

Follow this and additional works at: <https://scholarship.shu.edu/dissertations>



Part of the [Condensed Matter Physics Commons](#)

Recommended Citation

Kurywczak, Eric, "d-Orbital Occupancy of Transition Metal Oxides by X-Ray Absorption Near Edge Structure (XANES)" (2020). *Seton Hall University Dissertations and Theses (ETDs)*. 2765.
<https://scholarship.shu.edu/dissertations/2765>

d-Orbital Occupancy of Transition Metal Oxides by X-Ray Absorption Near Edge Structure
(XANES)

by

Eric Kurywczak

Submitted in partial fulfillment of the requirements for the degree

Master of Physics

Department of Physics

Seton Hall University

May 2020

© 2020 Eric Kurywczak

SETON HALL UNIVERSITY
COLLEGE OF ARTS AND SCIENCES
DEPARTMENT OF PHYSICS

APPROVAL FOR SUCCESSFUL DEFENSE

Eric Kurywczak has successfully defended and made the required modifications to the text of the master's thesis for the **M.S.** during this **Spring Semester 2020**.

MASTER'S COMMITTEE

(please sign and date beside your name)

Mentor:

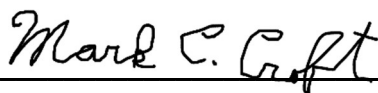
Dr. M. Alper Sahiner



(5/4/2020)

Co-Mentor:

Dr. Mark Croft



(5/1/2020)

Committee Member:

Dr. Erie Morales



(5/4/2020)

The mentor and any other committee members who wish to review revisions will sign and date this document only when revisions have been completed. Please return this form to the Office of Graduate Studies, where I will be placed in the candidate's file and submit a copy with your final thesis to be bound as page number two.

ACKNOWLEDGEMENTS

Thank you to Seton Hall University for being my educational home since my freshman year back in 2014, giving me the opportunity to obtain both a B.S. and now an M.S. in Physics. I am indescribably grateful for the M.S. program as I would not have been able to build the resume that got me into the PhD program at NJIT for the coming Fall 2020 semester onward. It was a great honor to be part of the first class of students in the program and being able to work on this project has been incredibly validating. I would also like to thank my family for the encouragement they have given me as a graduate student and pushing me to accomplish this goal and move on to a PhD program. Lastly, I would like to thank the Advanced Material Synthesis and Characterization Lab (AMSCL) under Dr. Sahiner's leadership and NSF-DMI 0420952.

TABLE OF CONTENTS

Acknowledgements.....	i
Abstract.....	iii
Introduction.....	1
- Transition Metals Oxides.....	2
- Literature Survey	3
- X-ray Absorption Near Edge Structure.....	13
- XANES Research.....	18
- An Example XAS (XANES & EXAFS)	20
- Curve Fitting Formula.....	22
Data Analysis.....	26
- Raw Data Normalization.....	26
- Results Breakdown.....	29
- 4 <i>d</i> Row Curve Fits.....	44
- 5 <i>d</i> Row Curve Fits.....	47
- The Arctangent Continuum.....	51
Error Analysis.....	54
Conclusion.....	55
References.....	57

ABSTRACT

XANES L_2 and L_3 -edge X-Ray Absorption Near Edge Spectra (XANES) for $4d$ and $5d$ row transition metals (TM) oxides are assumed to be directly reflecting unoccupied d orbitals influenced by the local symmetry of the metal ion. XANES L_2 - and L_3 -edge data analysis through non-linear curve fitting allows for a unique, efficient look at the structural eccentricities of transition metal oxides. In this way it is possible to determine the oxidation state of a material as well as its site symmetry. We have used non-linear least-squares fitting across the near-edge region of the various $4d$ row and $5d$ row TM oxides in order to investigate the systematics of the d -orbital occupancy and the XANES white line features for t_{2g} and e_g symmetry orbitals. The statistics have shown promising trends for $4d$ and $5d$ row level transition metal oxides. The systematics obtained with these results provide crucial information for the synthesis of new materials with specific electronic structures and crystal symmetries.

INTRODUCTION

Transition Metal Oxides:

Transition metal oxides (TMOs) have unique properties making them of particular interest in the field of solid state physics. TMs on their own are incredible and versatile materials with the ability to form highly stable complexes with a variety of other elements. Their defining characteristic, however, is that they have only partially filled d -orbitals making them somewhat odd as elements in the periodic table. Some compounds created using transition metals show superconducting and paramagnetic traits that are key to those working to develop the field of electronics and computing.¹ For the purposes of solid state physics research, the focus is on $4d$ and $5d$ TM oxides because of the existence of several overlapping energy scales and competing interactions present such as spin-orbit, coulomb and exchange interactions.¹ The crystal structure of a TMO is, of course, a relevant factor determining bonding properties as well as the symmetries that the electrons in the d -orbitals follow.

Transition metals' defining characteristic of having only partially filled d -orbitals is what makes them able to be thoroughly analyzed through x-ray absorption spectroscopy at a synchrotron facility. Specifically, the L_2 - and L_3 -edges of the spectra belonging to the near edge range can provide useful systematics about transition metal oxides. As the spectra is broken down into the L_2 - and L_3 -edges, the p to d -orbital transitions being analyzed can be broken into different symmetries consisting of the crystal-field states t_{2g} and e_g depending on the electron's energy. The t_{2g} state consists of the d_{xy} , d_{yz} , and d_{xz} orbitals while the e_g state consists of the $d_{(x^2-y^2)}$, and $d_{(z^2)}$ orbitals in octahedral environments.¹ Here the charge density of the e_g orbitals extends toward the filled-electron ligand sites (at the corners of the octahedra) raising its energy

while the t_{2g} charge density lobes extend toward the centers of the octahedra edges and have a lower energy. Elaborating on the difference between the L_2 - and L_3 -edges, the L_2 -edge outlines the transition from $p_{1/2}$ initial states to $d_{3/2}$ states while the L_3 -edge outlines the transition from $p_{3/2}$ initial states to $d_{5/2}$ final states.² Depending on how the transitions for the p -orbital electrons proceed, it is necessary to see which state they come to occupy as this will provide insight about the electronic properties of the sample material. Looking at several oxides composed of the same TM but with difference formal occupancy values, patterns regarding d -orbital filling can easily be observed providing a superior chance at understanding any TMO sample.

For the purposes of the research done here, the TMOs being analyzed are all perovskites following the ABX_3 crystal structure (A: cation, B: metal ion, and X: anion). The perovskite structure itself is based on that of calcium titanium oxide ($CaTiO_3$) and because of the crystal's octahedral structuring, is able to be easily rotated and tilted. The utility that perovskites have due to being flexible is paired with the capacity to tune their physical properties by replacing the cationic species located at the A- and B-sites.³ Being able to select the physical properties desired allows for a simplified synthesis of materials that act as insulators, conductors, or semiconductors. Ensuing from the ability to select preferred traits, the focus on perovskites comes out of research into ferroelectric materials for use in next generation computer hardware and photovoltaic cells. Knowing that perovskites are the subject material also means keeping in mind the electron orbital traits connected with such a structuring. In perovskites the orbital split between t_{2g} and e_g has the triply degenerate t_{2g} case being of lower energy compared to the doubly degenerate e_g with a sizeable energy gap between them. Ignoring this information would be remiss when analyzing XANES data, especially when the goal is probing the d -orbital

features present in the $L_{2,3}$ -edges of a spectra because it means the e_g orbitals are empty for each sample.

Literature Survey:

L_2 and L_3 measurements of transition-metal 5d orbital occupancy, spin-orbit effects, and chemical bonding²

Qi *et al.*² present the L_2 and L_3 x-ray absorption spectroscopy measurements for all of the 5d transition metal (T) elements and some TAl_2 intermetallic compounds looking for trends across the XANES spectra. A striking difference in white-line intensity exists between the spectra of Au and that for Ta following with the d -orbital occupancy across the 5d row. For Au there is an absence of a WL feature at both the L_2 - and L_3 -edges indicating that there are essentially no 5d holes in elemental Au. When it comes to Pt, however, there is a distinct difference between the WL features for the L_3 - and L_2 -edges. For the L_3 -edge the presence of the WL feature is evident while in the L_2 -edge, there is only a slight shoulder to suggest a remnant of a WL feature. This difference reflects spin-orbit-induced preponderance of $5d_{5/2}$ holes versus $5d_{3/2}$ holes in elemental Pt. Area estimates for the white-lines were done with the superposition of a Lorentzian for the peak and an arctangent for fitting the continuum. In order to support the calculations done in this way, the Au edge was taken and shifted to approximate the continuum absorption and subtracted away from the other edges. With the area values, a regular correlation between atomic number and the L_3 -edge area is evident with a similar trend being evident in the L_2 -edge area. When plotting the areas compared to atomic number, there is a decrease in area

following a decrease in atomic number. The ratio of the areas for samples reflects the previously mentioned spin-orbit splitting of the $5d$ band and its hole population. Consequence of these calculations, it is noted that the separate L_2 - and L_3 -edge areas can be used as separate estimates of the total $5d$ hole count.

XAS Studies of 1:2:2 Transition Metal Compounds⁴

Chen *et al.*⁴ conducted XANES analysis of $4d$ transition metal (T) compounds looking for anti-bonding features between a transition metal and a group IV or V element (X) above the Fermi level by hybridization. With these transition metals, the XANES spectra is dominated by an intense white-line feature indicating electrons from the $2p$ -core level to empty d -orbital states. The strength and splitting of the white-line feature decreased as they went through a sequence of different X from $\text{Si} \rightarrow \text{Ge} \rightarrow \text{Sn}$. The observations could have also been a result of a decrease in the T $4d$ states at the Fermi level relative to the elements. As part of the analysis process an L_3 -edge area vs. atomic number plot was made allowing for a determination of the expected WL area change for a $4d$ hole based on the plot's slope. In the end, the need for further theoretical treatment of the role of $4d$ states and T - X hybridization was showed along with how useful XAS is for electronic structure probing above the Fermi level.

Transition-metal (Au, Pt, Ir, Re) bonding to Al, Si, Ge: X-ray-absorption studies⁵

Jeon *et al.*⁵ discuss and correlate the strength of the white-line features at the L_2 - and L_3 -edges of a selection of T - X compounds where $T=\text{Au, Pt, Ir, and Re}$ and $X=\text{Al, Si, and Ge}$. In the

study they saw that the x-ray absorption spectroscopy results appear to offer a direct method of probing the transition metal $5d$ -orbital charge transfer. In the XANES spectra, a sharp Lorentzian-type white-line feature occurs a few eV before the onset of the continuum transitions. Since the WL feature rides atop the continuum step, it is necessary to subtract the continuum out in order to accurately estimate the area of the feature itself. By superimposing the Au $L_{2,3}$ -edge spectra with the spectra of other compounds allows for easy subtraction of the continuum step in order to obtain area values. An issue with this method is that differences in the fine-structure oscillations can contribute to the near-edge area difference potentially increasing or decreasing the WL-area estimates. These L_2 - and L_3 -edge WL area measurements offer a way of estimating $5d$ -orbital hole counts for the $d_{3/2}$ and $d_{5/2}$ states. In turn, the area measurements allows for better understanding the strength and character of a compound's bonding. The area values from the $L_{2,3}$ -edges track each other indicating a distribution of the d -orbital holes between the $d_{3/2}$ and $d_{5/2}$ states. Between the samples tested, the Al compounds seem to have more strongly reduced spin-orbit effects compared to the Si and Ge compounds. While looking for changes in the white-line area associated with bonding, the elemental white-line is subtracted away. This study was successful in proving the chemical bonding-induced charge-transfer effects of $T-X$ and 1:2:2 compounds. The researchers want to underline the limitations of the method of subtracting away the elemental Au spectra in order to estimate WL areas and the need to improve on this front. They also believe that this work offers a useful method of using XANES data to provide a window into local bonding strengths in compounds as well as being a test for theoretical models regarding such bonding.

X-ray-absorption near-edge structure study of $\text{IBi}_2\text{Sr}_2\text{CaCu}_2\text{O}_y$ ⁶

Liang *et al.*⁶ set about a XANES study of $\text{IBi}_2\text{Sr}_2\text{CaCu}_2\text{O}_y$ crystals. The study was split between the iodine L_1 -, bismuth L_3 -, and copper K -edges. The L_1 -edge represents the excitation of s -orbital electrons, the $L_{2,3}$ -edges are representations of p -orbital electrons being excited, and the K -edge represents excitation of $1s$ electrons specifically. Covering all of these segments of the XANES spectra gave a rounded understanding of the sample in question. For instance, the L_1 -edge results indicated that intercalated iodine layers receive electronic charges and that iodine $5p$ -orbital holes are in states oriented in the iodine plane itself. In the L_3 -edge there was an out-of-plane downward shift as well as an in-plane upward shift due to iodine intercalation. These shifts were for $6d-t_{2g}$ and $6d-e_g$ states caused by an octahedral to pyramidal shift of the Bi-O bond. This structural shift is backed up by the edge shift that is present upon iodine intercalation. In the copper K -edge did not show any significant changes as a result of the iodine intercalation. For the quantitative portion of the research, fitting was done by superposition of arctangent and Lorentzian-Gaussian combination to determine the area of the white-line features. The conclusion reached through this study, supported by the changes in the XANES spectra, was that intercalated iodine extracts charge from neighboring Bi-O layers and others.

*Large Effects of A-site average cation size on the properties of the double perovskites $\text{Ba}_{2-x}\text{Sr}_x\text{MnReO}_6$: A d^5-d^1 system*⁷

Popov *et al.*⁷ analyzed the XANES $L_{2,3}$ -edges' white line (WL) features to determine the local environment of several different samples. The samples in question were ferromagnetic

double perovskites that had gained interest due to the discovery of large, low-field, room-temperature magnetoresistance in $\text{Sr}_2\text{FeMoO}_6$. A starting goal of the XANES analysis for the samples was determination of the oxidation state. Beyond this, determination of the chemical shift of Re between the three tested double perovskites was conducted based on the centrum of the t_{2g} and e_g WL features. Also mentioned in this paper is the inverse connection between the intensity of the t_{2g} WL feature and d -orbital occupancy, which is an important variable to observe across XANES studies. The paper raps up having determined the formal oxidation states by x-ray absorption spectroscopy and successfully analyzed the ferromagnetic properties of the samples.

*XANES study of hydrogen incorporation in a Pd-capped Nb thin film*⁸

Ruckman *et al.*⁸ set out to use XANES as a tool for studying hydrogen incorporation in a Pd-capped Nb thin film. The XANES analysis showed that there are spectral changes related to Pd-hydride formation. The spectral changes include white-line feature degradation and the appearance of a Pd-H antibonding feature at 6 eV. Hydrogen charging of the thin film resulted in enhancement of white-line strength of the $L_{2,3}$ -edges. Such hydrogen charging has been shown to increase WL area and suppress superconductivity in metals. The new feature resulting from Pd-H antibonding is due to the scattering of outgoing photoelectrons by on-site hydrogen $1s$ states. The XANES spectra also confirmed that introducing hydrogen into Nb reduces p and d density of states at the Fermi edge. In regards to checking the density of states, the L_2 -edge is a better representation due to multiplet effects that interfere in the L_3 -edge. The conclusions made from the analysis was that much of the structural change upon introducing hydrogen to the 2400

angstrom thick Nb film is due to expansion of the lattice rather than metal-H bonding. The new features located at 6 eV above the absorption threshold are however attributed to such a bond.

*Electronic structure of the Fe–Cu–Nb–Si–B alloys by x-ray absorption spectroscopy*⁹

Cheng *et al.*⁹ measured the XANES spectra of nanocrystalline and amorphous FCNSB and FeSiB alloys at the $L_{2,3}$ -edges. The samples were compared to reference material spectra to see what changes occurred. The features in the Fe L_3 -edge of *nc*-FCNSB changed shape significantly upon addition of Cu and Nb to the FeSiB alloy. These changes indicated a strong influence of Cu and Nb on the Fe 3*d* local electronic structure, with close examination of the Cu $L_{2,3}$ -edge indicating that the copper clusters have a body-centered-cubic structure. In order to determine the changing of 3*d* electronic structuring for FCNSB between *nc*- and *a*- samples, it is necessary to know that the area beneath the white-line features is a convolution of the transition matrix element and the unoccupied density of states. A source of difficulty when analyzing the 3*d* row $L_{2,3}$ -edge spectra is that they contain complicated multiplet splittings, where *p*-hole spin couples with *d*-electron spin. Some WL features at the Nb L_3 -edge suggested a slight increase in the delocalization of Nb 4*d* orbits when *a*-FCNSB is crystallized into *nc*-FCNSB. The main feature of the L_3 -edge showed a decreased intensity compared to the Nb reference metal with this lower feature indicating fewer unoccupied Nb 4*d* states and the delocalization of the 4*d* orbitals mentioned previously. All of this came together to adequately present the changes that occur between *nc*- and *a*-FCNSB.

X-ray-absorption studies of the d-orbital occupancies of selected 4d/5d transition metals compounded with group-III/IV ligands¹⁰

Jeon *et al.*¹⁰ used the XAS of several 4d/5d transition metals to explore the systematic variations of their *d*-orbital occupancy in *T-X* compounds. In order to quantify the changes in the *d*-orbital occupancy, the strength of the white-line features at the *T L*_{2,3}-edges were used. The precise role of *d*-orbitals in bonding in transition metal compounds depends on the details of local symmetry, ligand field strength, and other electronic structure parameters. The most important features analyzed in the *L*_{2,3}-edges are the *d*-hole related white-line feature and the step-shaped continuum feature. The last transition metal in the 4*d* and 5*d* rows was used as a means to subtract away the continuum component and analyze the WL feature. This is done by superimposing it over the XANES spectra for the sample being analyzed. Although there are shortcomings of this method, it is simple to apply and effective despite the potential flaws incurred through its use often leading to underestimation. There exists a linear correlation between the areas of the *L*₂- and *L*₃-edges and atomic number between Ag and Mo. Linear least-squares fitting was conducted on the XANES data yielding average WL area change between adjacent 4*d* elements. As a way to simply parameterize the changes in net *d*-orbital population between materials, the average area is used. When looking at the XANES spectra for 5*d* compounds, the strength of the WL feature decreases as *X* goes down the column from Al → Ga → In. This detail supports the notion that the ability of the *X* element to create *T 5d* holes will decrease along that sequence.

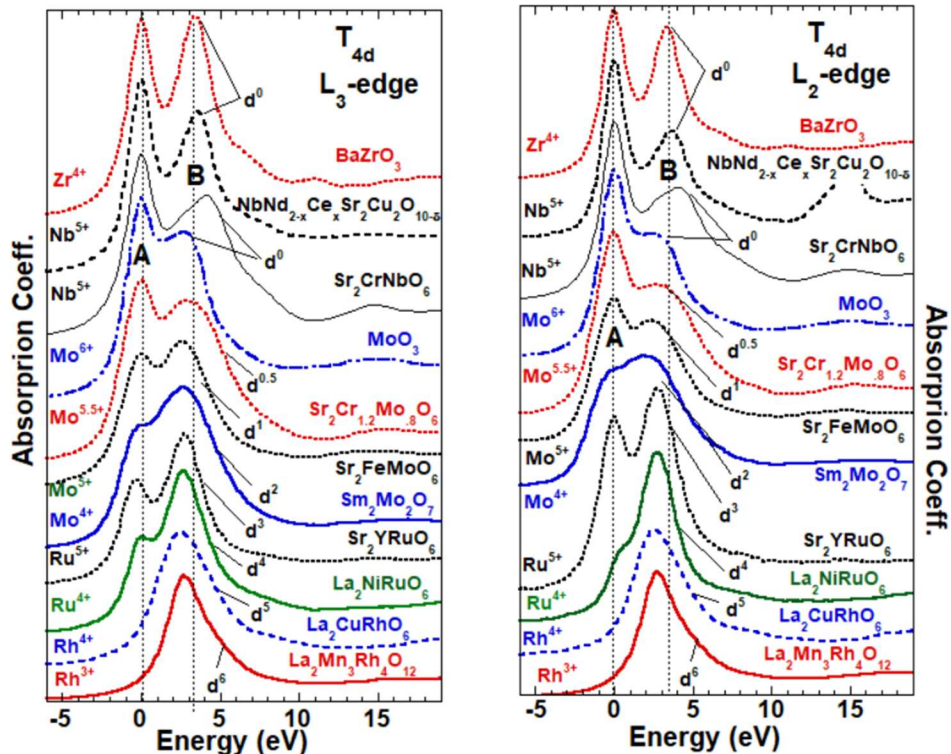
Relationship between the area of $L_{2,3}$ x-ray absorption edge resonances and the d orbital occupancy in compounds of platinum and iridium¹¹

J. A. Horsley¹¹ set out to conduct a XANES study on compounds of platinum, iridium, and their pure metal variants in order to determine a relationship between the white-line intensity and d -orbital occupancy. Rather than using the L_3 -edge alone to look to see the same trend, both the L_2 - and L_3 -edges were going to be analyzed. The relationship in question is important due to the charge shifts caused by the presence of core hole on the metal being constant for different ligands and therefore has broad application. In order to obtain the area values for the WL features of the L -edges to determine the relationship, a combination of Lorentzian and an underlying continuum component were utilized. Unsurprisingly, the relationship was observed in the L_3 -edge but Horsley was also successful in showing it in the L_2 -edge, which was a core goal of the study. The process could not be applied to IrO_2 because of the absence of transitions to empty d states at the top of the valance band. The results themselves were positive across the L -edges area values, showing the desired relationship to d -orbital occupancy. Problems did come up when attempting to extend the relationship from platinum to other noble metals such as iridium and osmium for the previously mentioned reasons coming out from transitions to unoccupied d states at the top of the valance band.

The Original Data

The XANES $L_{2,3}$ data being analyzed comes from several different files created by Dr. Mark Croft of Rutgers University over many years. The XANES data itself was obtained at the

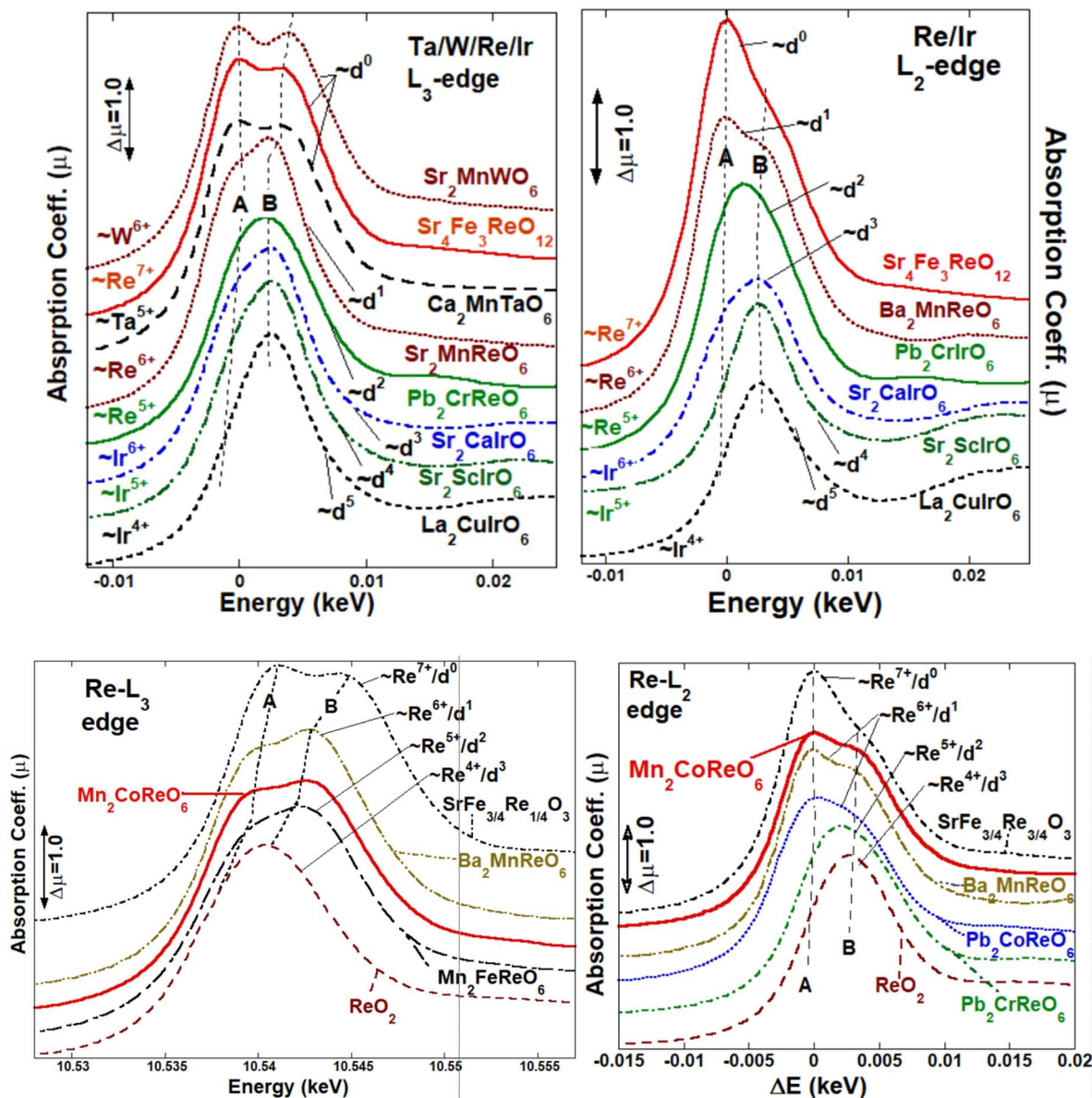
National Synchrotron Light Source (NSLS and NSLS-II) of Brookhaven National Laboratory (BNL). The TMOs that were tested come from across the 4*d* and 5*d* rows. The 4*d* row XANES data was the first set to undergo the curve fitting process as a testbed before beginning work on the full collection provided.



Figures 1 & 2: Depicted are the white-line features of the L₃-edge (left) as well as the L₂-edge (right). In both, the formal *d*-orbital occupancy of each transition metal oxide is given going from a filled *t*_{2g} orbital with *d*⁰ at the bottom of each plot, to *d*⁰ at the top. With La₂Mn₃Rh₄O₁₂ the absence of empty *t*_{2g} holes should mean there is only *e*_g contribution. (Images from KaleidaGraph)

Looking at the 4*d* row alone in figures 1 and 2, there was evidently going to be a sizeable selection of resulting values from the curve fits to sort through and compare. For the remaining XANES data to be analyzed we look to a collection of 5*d* TMOs shown in figures 3 through 6

with a focus placed on the compounds containing rhenium as they made up the bulk of the XANES data.



Figures 3-6: L₃-edge (left) and L₂-edge (right) datasets for the 5d row transition metal oxides focused on the white-line features. Formal *d*-orbital occupancy of each compound is also shown. This set has less pronounced splitting between the *t*_{2g} and *e*_g final states compared to the 4d row samples. (Images from KaleidaGraph)

X-ray Absorption Near Edge Structure:

As a technique, x-ray absorption near edge structure (XANES) came out of the full x-ray absorption spectra (XAS) along with the more commonly analyzed extended x-ray absorption fine structure (EXAFS). X-ray absorption measurements of this type conducted at synchrotron facilities got their start at Stanford Synchrotron Radiation Laboratory in 1974.¹² The setup itself for these experiments is straightforward despite requiring a massive investment to construct the infrastructure alone. The most important and sizeable piece is the synchrotron ring itself where charged particles are accelerated resulting in the emission of x-ray radiation that is then collimated and focused before impacting a sample to be analyzed. When an experiment requires a particular wavelength be used, the apparatus can also narrow down the radiation sent through to that wavelength.¹³ As for why the synchrotron ring is the key piece of equipment, it allows for the production of incredibly bright x-rays that while having high intensity also has the low emittance required for conducting experiments in the field of XAS.¹⁴ The utility and versatility of synchrotron laboratories paired with their limited numbers makes obtaining beam time to conducted experiments highly competitive. Once an experiment has been conducted, however, the results will come out in files that can be brought into the commonly used absorption versus energy plots used in the field for analysis. The absorption coefficient used and the energy range that is covered will depend on the material being tested.

In XAS experiments the key event being observed is electron excitation and transition. X-rays incident on a sample will transfer energy resulting in electron transitions from lower atomic energy levels to higher levels.¹⁵ In the case of XANES $L_{2,3}$ -edge observations, the transitions are from the p -orbital to the d -orbital. Following the free electron relation

$$\frac{p^2}{2m} = h\nu - E_0$$

and Fermi's Golden rule, where W is the total transition rate,

$$W = \frac{2\pi}{\hbar} \left(\frac{eE_0}{2} \right)^2 |\langle i|z|f \rangle|^2 \rho(E_f) \quad (2)$$

it is possible to predict and understand how these transitions occur. In Fermi's Golden rule, $\rho(E_f)$ is the density of final states at a particular energy where $|i\rangle$ is the initial state and $|f\rangle$ is the final state. Following the transition event, electrons will shortly drop down to fill the lower energy levels resulting in the emission of radiation and/or the expulsion of Auger electrons depending on how much energy is released.¹⁵ For the purposes of this project, the detection method used is reliant on analysis of the transmitted energy through a sample using two ionization chambers to detect the initial flux (I_0) and the transmitted flux (I_t). Between samples and depending on whether the XANES or EXAFS regions are being analyzed, varied beam energies will be required. To allow for this flexibility in experiments, a monochromator is used at synchrotron sources making it possible to tailor an x-ray simplifying the process of obtaining useable data.

For a more expansive mathematical take on the x-ray transition rate it is common to derive the equation through the use of the one-particle Green's function. The transition rate equation found is equivalent to the previously shown Golden Rule formulation (2), however, the one-particle Green's function describes the excited electron states.¹² To properly show the process of deriving the x-ray transition rate in this way, *X-Ray Absorption: Principles, Applications, Techniques of EXAFS, SEXAFS, and XANES* by D. C. Koningsberger and R. Prins does a fantastic job beginning with the Hamiltonian:¹²

$$H = H_0 + H'$$

where H_0 is the Hamiltonian for the electron plus unoccupied photons and H' is the electron-photon interaction.

$$H' = \frac{e}{c} \int dr j(r) * A(r) + \frac{e^2}{2mc} \int dr \rho(r) A^2(r) \quad (3)$$

Here $\rho(r)$ is the electron number, $j(r)$ is the current density, and $A(r)$ is the vector potential where in x-ray absorption only the first term is used while the second is applied for higher-order processes like x-ray scattering.¹² For further progress an evolution operator is needed and it comes in the following form:

$$U(t) = e^{-iH_0 t} \quad (4)$$

and a particle state of

$$|\psi(t)\rangle = -i \int_0^{t_0} dt U(t_0 - t) H' U(t) |c, q\rangle$$

with $|q\rangle$ being the photon state and $|c\rangle$ being the core state having an eigenvalue ϵ_c . The probability that at t_0 the photon has been absorbed and the excited electron is in state $|n\rangle$ will be equivalent to

$$P_n(t_0) = |\langle n | \psi(t_0) \rangle|^2 \quad (5)$$

and upon summing over the final states $|n\rangle$ gives a total transition rate of

$$W = \frac{d}{dt_0} \left\{ \lim_{t_0 \rightarrow \infty} P(t_0) \right\}$$

Introducing Green's function containing the complex variable z

$$G(z) = (z - H_0)^{-1}$$

which is related to the evolution operator by

$$U(t) = -\frac{1}{2\pi i} \int_{-\infty}^{\infty} dx e^{-ixt} (G^+(x) - G^-(x)) \quad (6)$$

Combining the evolution operator with the probability equation (5),

$$W(\omega) = -2\langle c|h^*\text{Im } G^+(\varepsilon_c + \omega)h|c\rangle \quad (7)$$

which is our fundamental expression for the transition rate where

$$h = \frac{e}{c} \int dr j(r) \cdot A_q^\lambda e^{iq \cdot r}$$

is an operator on the electron states only and $A_q^\lambda e^{iq \cdot r}$ is the expectation value of the vector potential in photon state $|q\rangle$. In order to show the equivalency to the Golden Rule it is necessary to insert the eigenfunction expansion of Green's function:

$$G^+(\varepsilon) = \sum_n \frac{|n\rangle \langle n|}{\varepsilon - \varepsilon_n + i\eta} \quad (8)$$

thereby producing,

$$W(\omega) = 2\pi \sum_n |\langle n|h|c\rangle|^2 \delta(\varepsilon_c + \omega - \varepsilon_n)$$

Having now gone through this derivation an explanation as to why it has been done is in order. As a primary motivation, the Green's function method allows for the ready implementation of multiple-scattering theory that is pivotal to XANES theory as a whole. Being able to make contact with the many-body phenomena that are inherent to the XANES features allows for a significantly improved grasp of what is occurring in a sample during analysis contributing to an effective implementation of any results and the sidestepping of errors in interpretation.

To bring the theory into practice, XAS plots are made in the form of absorption versus energy but what has been shown in the previous derivation is not able to do so in its current state. To make the change over to absorption coefficient rather than total transition rate and understand how the transitions are analyzed, the first step is considering the power being absorbed from the electromagnetic wave per unit volume such that

$$(9)$$

$$\frac{du}{dt} = 4\pi^2\omega e^2 N_a u |\langle i|z|f \rangle|^2 \rho(E_f)$$

where N_a is the number of atoms per unit volume. Following from this we have the definition

$$\frac{du}{dx} = -\mu u$$

providing us with the absorption coefficient in the form of

$$\mu = \frac{4\pi^2\omega e^2}{c} N_a |\langle i|z|f \rangle|^2 \rho(E_f) \quad (10)$$

where it can be seen how the transition rate and absorption are related. This can be further manipulated into the final form that we are looking for

$$\mu(E) = \sum |\langle i|\hat{H}|f \rangle|^2 \rho(E_f) \quad (11)$$

where \hat{H} is the dipole/quadrupole operator. As for the absorption coefficient that will be plotted versus beam energy, $\mu(E) = \ln\left(\frac{I_0}{I_t}\right)$ will be used.

Returning to study in the field of XAS generally, EXAFS analysis became predominant due to its relative simplicity, speed, and because it gives practical information about the local structure of each atom in a sample. In comparison, XANES is more challenging to obtain useful results from but is potentially the more detailed segment of XAS data, providing important information such as the oxidation state, coordination geometry, and electron orbital occupancy. These strengths of XANES analysis make for an excellent tool when studying more complicated materials. As mentioned previously, looking into the p to d -orbital transition of transition metal oxides by analyzing the L_2 and L_3 -edge features is of significant interest. In XANES, the features being broken down are the peaks in absorbance vs energy, historically known as “white lines” due to the unexposed line on the photographic tape that was used to record the XAS, and the continuum that closes out both edges.¹² Through careful analysis the d -orbital occupancy and

chemical shift can be determined based on the white line areas. Conducting experiments over the XANES range are not as easy as for EXAFS requiring far greater accuracy from the data as even the slightest deviation can have compounding negative effects.¹²

A part of XANES' significance is connected to multiple scattering that occurs within a sample during an experiment. This multiple scattering is the main physical effect that determines the XANES spectra of condensed matter systems giving multiple scattering resonances that, along with shape resonances, provide the origins for the XANES peaks.¹² To elaborate, any sample undergoing XANES analysis has closely packed atoms depending on the chemical composition and the auger electrons and emitted photons will scatter amongst them. Accordingly, even slight changes in the structure of a sample will alter the spectra making it is possible to obtain detailed information about the orientation of the composite atoms. The extent to which multiple scattering influences XANES is why experiments need to be finely tuned and executed in order to obtain data that accurately reflects a sample.

XANES Research:

XANES research is focused on obtaining an in depth analysis of the electronic structure of a sample to better understand its properties. This information proves useful as far as developing new materials to either replace less effective ones or be applied in unique ways to further technological development. For this project in particular, the primary concern is quantifying the *d*-orbital occupancies of a varied set of TMOs from both the 4*d* and 5*d* rows. In order to have simplified analysis process that has suitable accuracy, it is necessary to create a formula for and conduct non-linear least squares curve fitting on the extensive collection of

XANES $L_{2,3}$ -edge spectra. The fitting process was undertaken in a variety of programs including KaleidaGraph, Mathematica, and Origin in order to gauge reproducibility across different programs. The most important pieces of information obtained through the fitting process are the area values for each peak in the L -edges. These area values correspond directly to the occupancy of the t_{2g} and e_g orbital symmetries in each TMO. To be specific, the area values provide an understanding about how empty the orbital is in each symmetry with a larger peak in one signaling that there are less occupied states in that segment of the d -orbital. This will be reflected in the area difference between the peaks in the $L_{2,3}$ -edges with cases where the second peak in each edge is larger than the first corresponding to more empty e_g orbital spaces. A smaller peak indicates less available occupancy which can be explained by taking into account that the XANES spectra is looking at the excitation of electrons from the p -orbital to empty slots in the d -orbital, which will shortly thereafter fall back down in energy. When later observing the area differences between each peak, it is far easier to understand the splitting between t_{2g} to e_g and the occupancy therein when comparing to known trends. In the perovskite structures being analyzed, for instance, the t_{2g} orbital typically fills before e_g due to inherit orbital energy differences between them.¹ In the event of a spectra where this is observed to not be the case, for instance, further inspection would be warranted to determine what led to this anomaly. Comparing across formal occupancy will also present any relevant trends between samples. The area values being collected therefore are the key results when determining the efficacy of the curve fitting process.

As for the continuum portion that follows each L -edge, they are a collection of unbound states with high kinetic energy that the WL is superimposed over.¹⁵ These unbound states separate themselves from the WL features because of the Columbic interaction between the p -holes and d -electrons resulting in the shift to lower energy creating the WL features. Compared

to EXAFS, where the continuum is the focal point of analysis, in XANES, the continuum needs to be recognized to accurately determine the step-up from the pre-edge to the post-edge. For the purposes of XANES research, the continuum is model through the use of an arctangent function. Frequently, the continuum will be subtracted out by superimposing a reference material with a full d -orbital on the spectra being analyzed. There is, however, no current consensus on where the inflection point that creates the pre- to post-edge step occurs when approaching it mathematically.

An Example XAS (XANES & EXAFS):

The whole XAS, as previously mentioned, can be broken into two distinct portions, XANES and EXAFS. As has also been mentioned, at what energy the split occurs depends on the sample being tested but is essentially the same across all XAS.

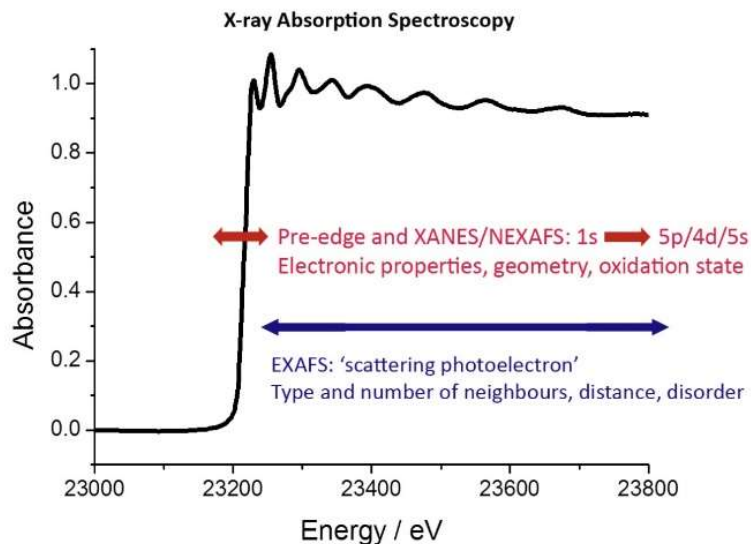
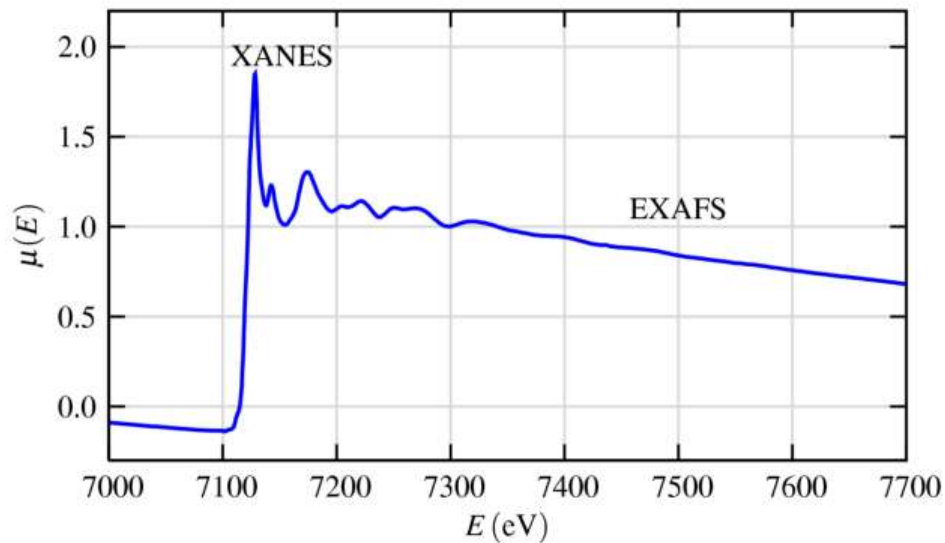


Figure 7: This example of an XAS does not have any prominent WL features in the XANES region, which are what researchers are focused on analyzing.



Figures 8: This example XAS show the difference between the XANES and EXAFS regions, particularly the appearance of each and how it differs in terms of absorption fluctuation

The example XAS of figures 7 and 8 differ in that figure 7 has been normalized and lacks a proper WL feature unlike figure 8, which does not appear to be normalized but has WL features that have appeared in and to are unique to the XANES region. The EXAFS region's fine fluctuations are also noticeable between both figures. These fluctuations are what EXAFS researchers analyze along with modeling results in order to determine the fine structure of a sample. In the figures, the split between the L_3 - and L_2 -edges are not made clear but can be seen well in figure 9.

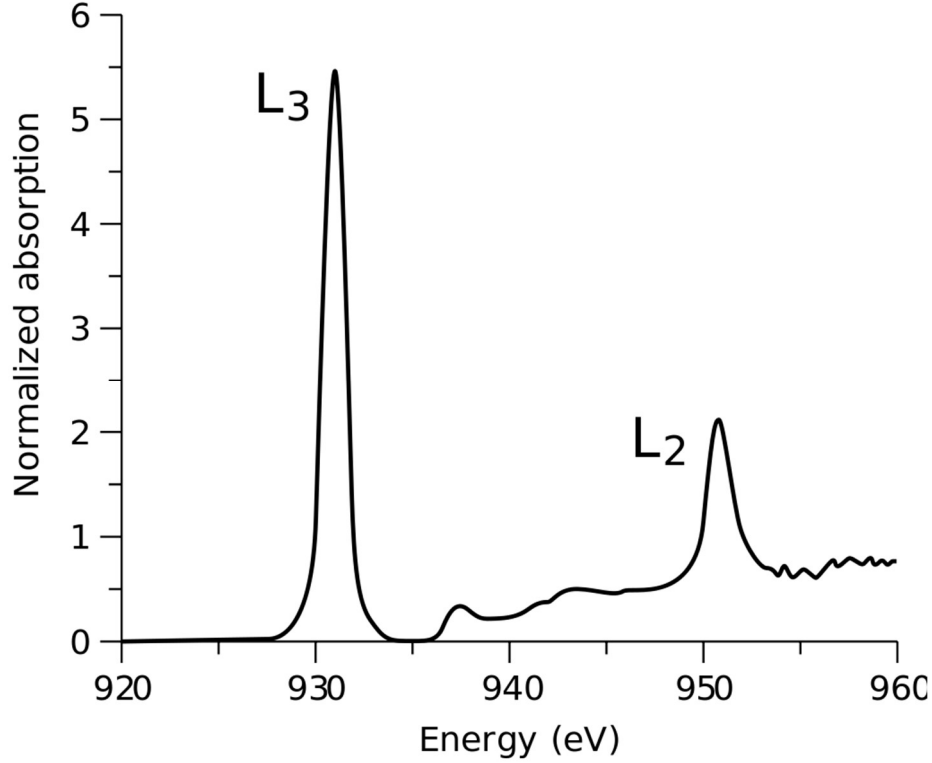


Figure 9: The split between the L_3 - and L_2 -edges is tied to the difference between the $d_{5/2}$ and $d_{3/2}$ electron states respectively.

With the two L -edges shown in figure 9, there is a significant absorption intensity difference between them with the L_3 -edge being the more pronounced of the two. As has been mentioned, the L_3 -edge consists of the electrons that jumped from $p_{3/2}$ initial states to $d_{5/2}$ final states while the L_2 -edge is made up of the electrons that jumped from $p_{1/2}$ initial states to $d_{3/2}$ final states. It is important that both edges are subjected to curve fitting analysis because the resulting trend should have agreement in regards to the d -orbital occupancy of the sample. Another difference between the edges that will become clear when looking at the fits later is that the split between the t_{2g} and e_g states is more pronounced for the L_3 -edge allowing for a simpler time fitting the higher energy samples at that edge.

Curve Fitting Formula:

When attempting to fit the XANES data, the best starting point was to break down the simplest spectra without factoring in the continuum portion, solely focusing on the peak itself and figuring out what distribution fit it best. The first attempts at getting fit results were made using the Gaussian distribution:

$$y = y_0 + \frac{A}{w\sqrt{\pi/2}} e^{-2\frac{(x-x_c)^2}{w^2}} \quad (9)$$

Almost immediately after the first attempts, the Gaussian was shown to be an ineffective mathematical tool to use. The reason for this was that the Gaussian had too sharp of an onset resulting in a far narrower peak than the XANES data being fit. In order to resolve the issue and achieve a more accurate fit, the transition to using a Lorentzian distribution was made.

$$y = y_0 + \frac{2A}{\pi} \frac{w}{4(x - x_c)^2 + w^2} \quad (10)$$

The Lorentzian's broader tails allowed for a significant improvement in fitting accuracy paving the way for the incorporation of an arctangent equation to capture the continuum, rounding out the curve fitting formula.

$$y = y_0 + h * \arctan\left(\frac{(x - x_{int})}{w}\right) \quad (11)$$

The arctangent itself was trivial to incorporate with variables such as step height and step width having a consistent range of acceptable values. As a new conundrum, the question of fitting cases with two distinct peaks came about. This inevitable predicament would rationally be solved by simply smashing two Lorentzian equations together along with an arctangent component to cover the continuum:

$$y = y_0 + \frac{2A_{t_{2g}}}{\pi} \frac{w_{t_{2g}}}{4(x - x_{t_{2g}})^2 + w_{t_{2g}}^2} + \frac{2A_{e_g}}{\pi} \frac{w_{e_g}}{4(x - x_{e_g})^2 + w_{e_g}^2} + h * \arctan\left(\frac{(x - x_{int})}{w}\right) \quad (12)$$

In order to have the two-peak XANES equation function properly, preliminary fitting statistics would be needed as attempting to blindly use this function proved to be wildly inaccurate. As an early stage of getting these preliminary parameters, the XANES data was windowed such that only one peak was contained per set and the continuum was cut out as a separate entity as well. This was done in order to do simpler fits on each component at individual stages. Once the separate, component fits were completed, the variables from them would be used as a guideline for the total XANES fitting function. For early fitting results, this method was incredibly effective, providing encouraging results that showed great promise for the endeavor being undertaken across the whole XANES data set being worked with.

Early, haphazard attempts at using equation (12) for fitting purposes where all of the variables were left floating provided some pleasant looking fits but they did not adhere to the traits inherent to the $L_{2,3}$ -edges being analyzed. Because of this, the next step became nailing down what values could be standardized. The values targeted for standardization came from the arctangent continuum portion of the XANES function being used. The easiest variable to set in stone was the height that the arctangent would have. The height ended up being fixed to $1/\pi$ in order to match the step height that came out of normalizing the raw synchrotron XANES data. Next up was the width of the arctangent, which has been made equal to the half-width of the e_g feature's Lorentzian. For the time being the inflection point of the arctangent was allowed to float to the right hand side of the e_g feature with the goal of minimizing its influence on the values for that second Lorentzian. It is uncertain whether the inflection point should be at a fixed

distance past the e_g feature or if it does, in fact, float around a particular range. The standardization of the arctangent portion of the XANES fitting function adjusted equation (12) into the following:

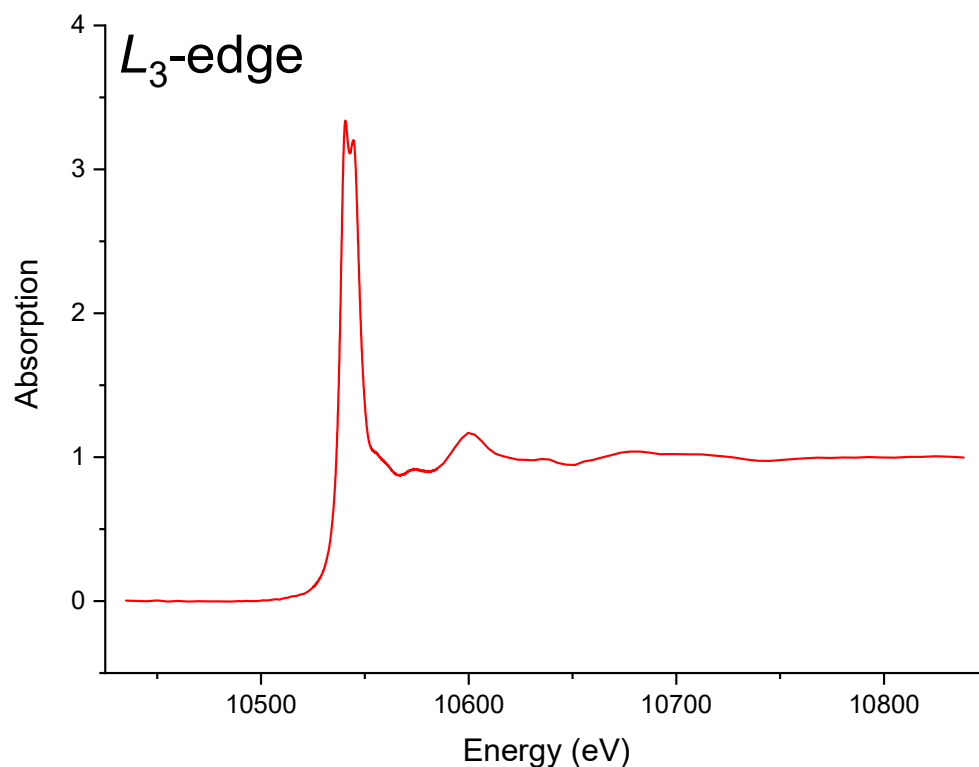
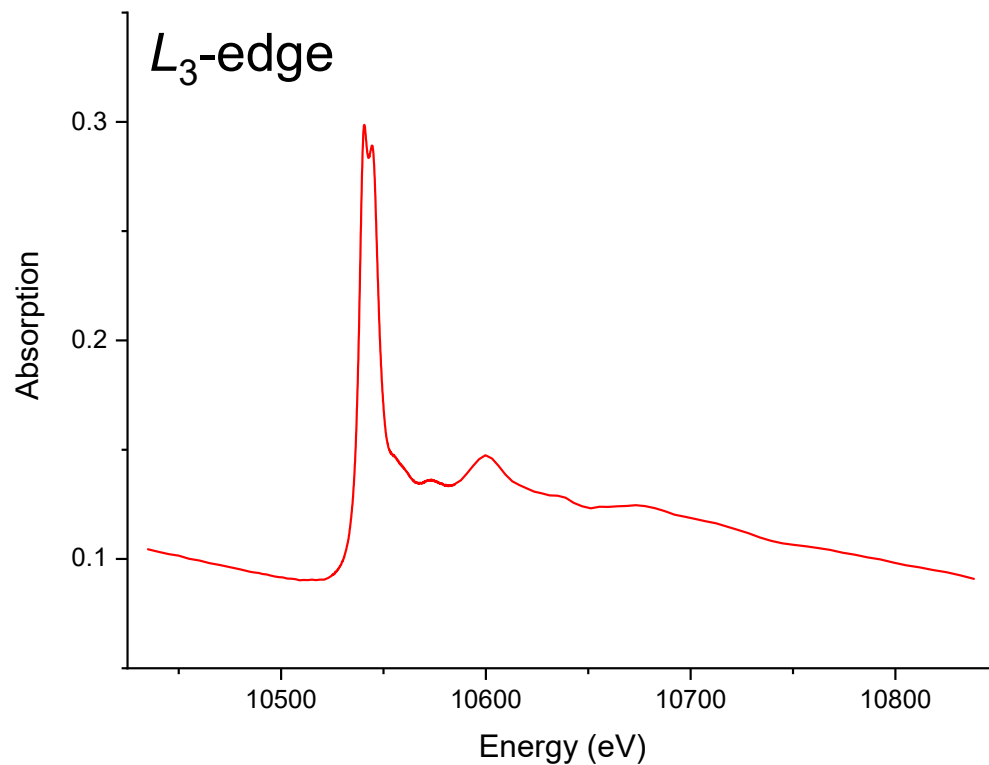
$$y = y_0 + \frac{2A_{t_{2g}}}{\pi} \frac{w_{t_{2g}}}{4(x - x_{t_{2g}})^2 + w_{t_{2g}}^2} + \frac{2A_{e_g}}{\pi} \frac{w_{e_g}}{4(x - x_{e_g})^2 + w_{e_g}^2} + \frac{1}{\pi} * \arctan\left(\frac{(x - (x_0 > x_{e_g}))}{w_{e_g}/2}\right) \quad (13)$$

Of course, the most important part of the whole process are the resulting values. That will be discussed in depth later but it is key to mention here that throughout the fitting process it is pivotal to pay attention to the pattern the Lorentzian areas follow. For instance, if one white-line feature is clearly larger than another, it would be illogical to keep results showing the opposite is true. The potential for such an occurrence is why determining the parameters of the arctangent was pivotal to obtaining accurate results. Before fixing the values of the arctangent, there were several instances where the floating variables would come together to provide pleasant looking fits with entirely incorrect resulting values.

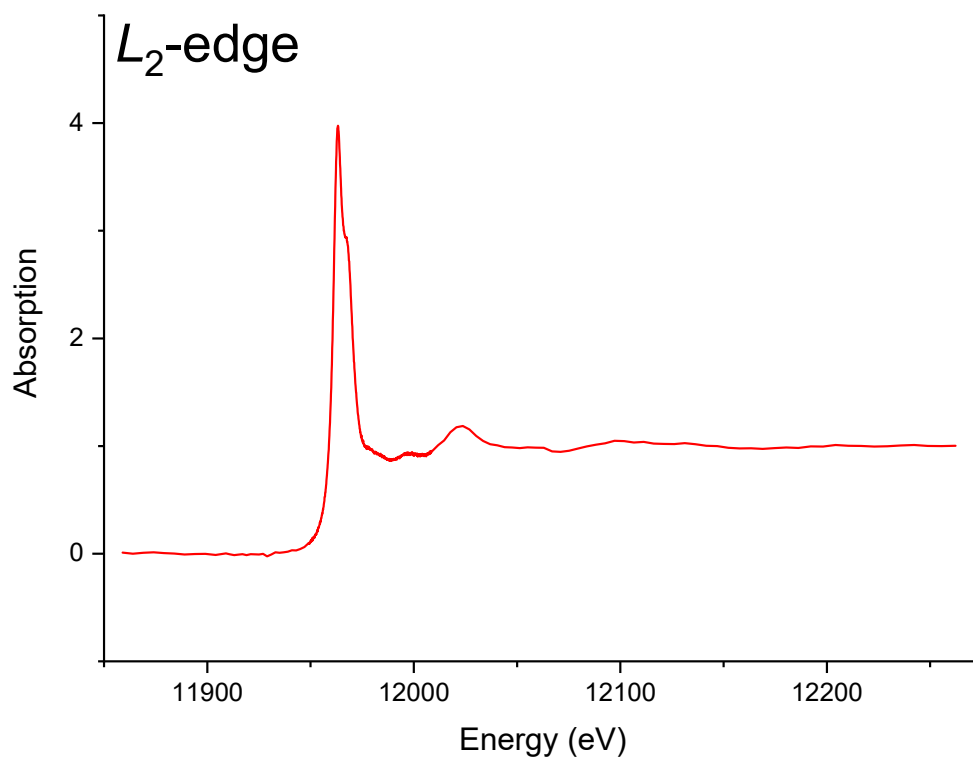
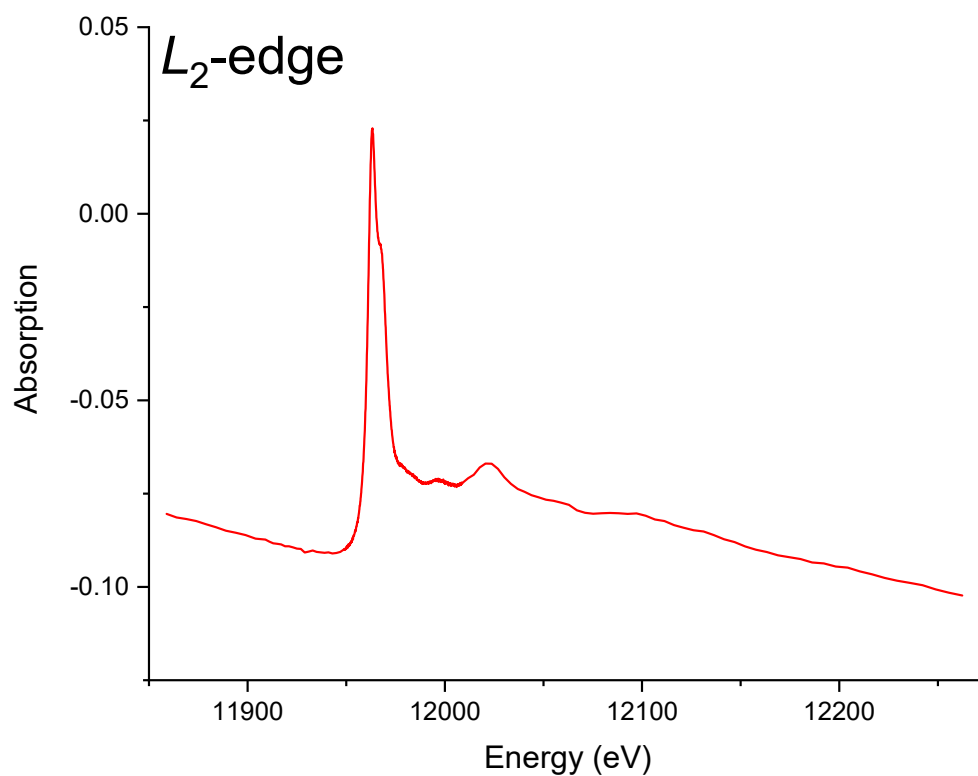
DATA ANALYSIS

Raw Data Normalization:

After sending a sample through the synchrotron, raw XANES data in the form of initial intensity, transmitted intensity, and reference intensity was obtained. This raw XANES data is the first place where the white-line for each sample will be noticeable. The problem is the XANES data needs to be cleaned up, or in other words, it needs to undergo normalization. The images in Figures 7 through 10 depict the raw XANES data alongside the normalized form illustrating the differences between the raw x-ray absorption coefficient, $\mu = \ln\left(\frac{I_0}{I_t}\right)$, plot and the normalized XANES data that is used for non-linear least squares curve fitting purposes. Here the I_0 is the current in the ionization chamber in front of the sample and measures the photon flux incident on the sample. I_t is the current in the ionization chamber after the sample and measures the photon flux “transmitted” through the sample. Programs such as WinXAS make the importation of the raw photon-energy, I_0 and I_t , routine as well as the fitting of the pre-edge background and post edge region for normalization with an example of original XANES data and normalized XANES data shown in figures 10 through 13.



Figures 10 & 11: $\text{Sr}_4\text{Fe}_3\text{ReO}_{12}$ raw XANES data (top) compared to the background subtracted and normalized XANES data (bottom) for the L_3 -edge showing the difference between the two, producing the step from pre-edge to post-edge which has been normalized to unity. (Images from WinXAS)



Figures 12 & 13: $\text{Sr}_4\text{Fe}_3\text{ReO}_{12}$ raw XANES data (top) compared to normalized XANES data (bottom) for the L_2 -edge. Note that the background subtraction and normalization have been applied. Again the step height is normalized to unity and the background

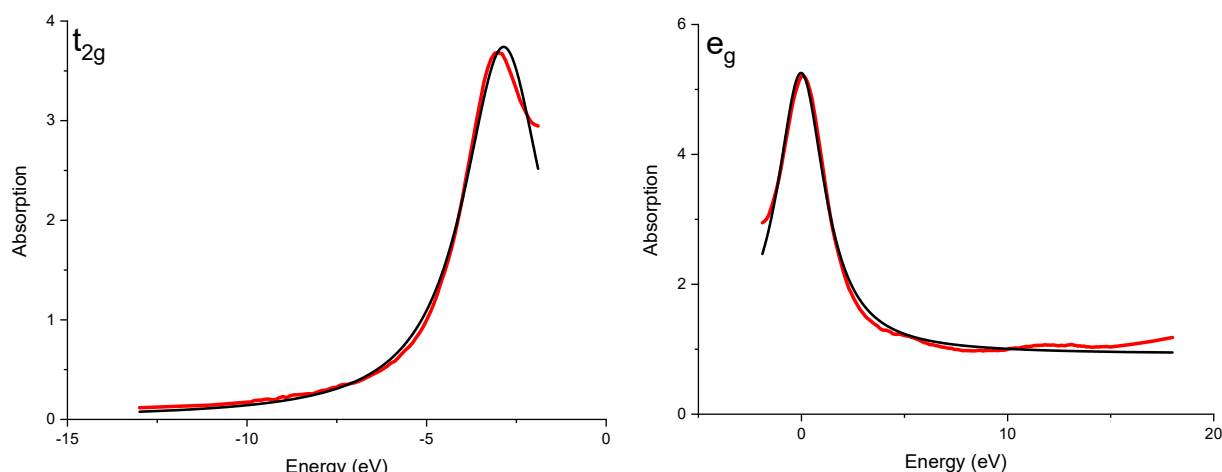
(non- L_2 -edge related) signal has been subtracted yielding zero in the pre-edge region. (Images from WinXAS)

The background subtraction and edge step normalization is routine, consisting of the importing the $\ln\left(\frac{I_0}{I_t}\right)$ raw XANES data, followed by processing that can be broken into two parts. First a polynomial fit (typically linear) is made to the background well below the edge and the fit is subtracted away. Then another polynomial fit is made to the XANES data well above the edge and the average of the two polynomial fits is normalized to unity. The polynomial fits in WinXAS only requires selecting the portions of the XANES data that are to be fit with the polynomials, clicking “fit” to make sure everything looks good, and then clicking “okay” to get the final product. At this point it is worth mentioning that I did not do the normalization step for the XANES data used for this project beyond one example set to provide insight about the process.

Results Breakdown:

At the onset, it is useful to discuss some of the procedure involved approaching the nontrivial multicomponent XANES data fitting. The fits were originally attempted in KaleidaGraph before moving over to Mathematica, which is a program I am more familiar with since it was used frequently in my undergraduate studies. After having done the fits in Mathematica, it was decided that Origin could prove more convenient for analyzing the XANES data. The first step in the fitting technique itself comes down to determining the small portion of each file that corresponded to the L -edge in question. This process is known as windowing and is absolutely necessary to ensure that only the relevant near edge features are being analyzed by the

curve fitting function discussed previously. Having windowed the XANES data, it was helpful to cut it into two segments (one t_{2g} and one e_g) in order to obtain preliminary parameters for our fitting equation by applying a Lorentzian fit (10) to these two segments. Examples of the split fits are shown below in figures 14 and 15.



Figures 14 & 15: Sr_2YRuO_6 L_3 -edge data (red line) and fits (blue lines) for the separated t_{2g} peak (left) and e_g peak (right) used for preliminary parameters. (Images from Origin 2019b)

These values cannot be used directly in analyzing the t_{2g} and e_g WL features because of the overlap that will occur. The ensuing overlap is corrected for by using the parameters obtained by these “split fits” as guides for the complete fitting function (13). Depending on the program being used, the way of guiding the fit will vary with a purpose built program such as Origin having a window in the curve fitting tool where the values can be input for each variable also allowing for variables to be easily pinned at a particular point when needed. Once the fitting function has done its work, results can be gathered and a visual representation such as figure 16 can be obtained.

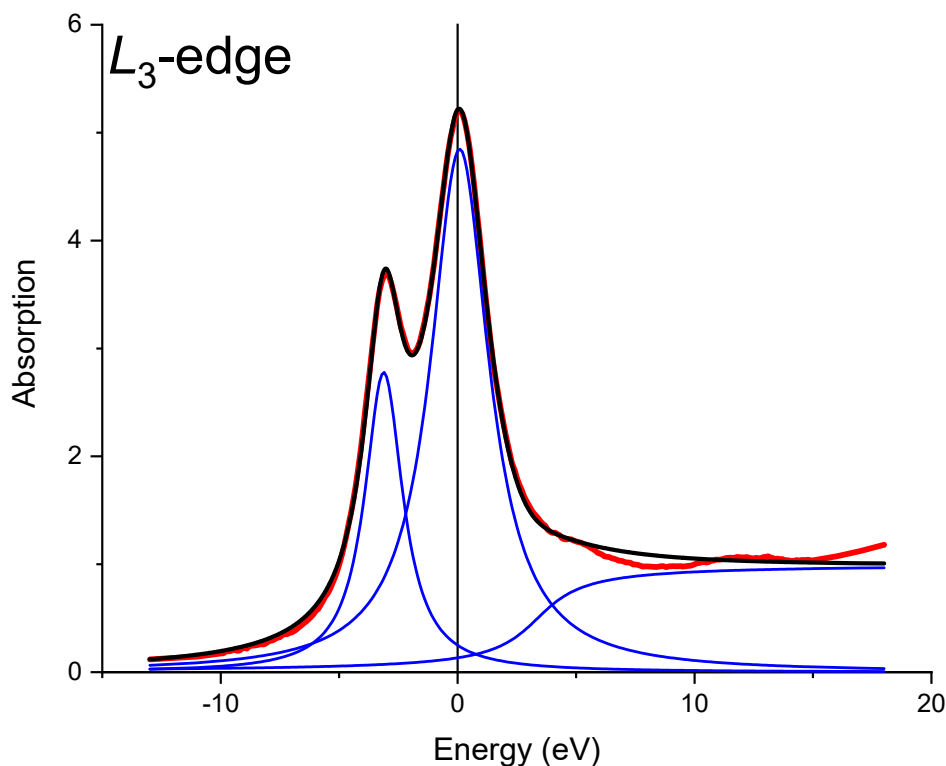


Figure 16: Sr_2YRuO_6 L_3 -edge final product (black line). Also shown are the final t_{2g} , e_g , and continuum components of the fit (blue lines) (Image from Origin 2019b)

This process was applied across both the $4d$ and $5d$ row data with the resulting values being compiled for further analysis, looking specifically for a correlation between the t_{2g} and e_g areas and d -orbital occupancy. The correlation between the areas should support the recognized d -orbital filling pattern of t_{2g} being occupied before the higher energy e_g in octahedral structured compounds. The significant problem throughout the fitting process turned out to be defining the arctangent continuum for the aforementioned reason that it directly influences the values of both Lorentzians but more so the values attributed to the e_g feature's Lorentzian, which will be explained in a later section devoted to the arctangent.

Comparison of the t_{2g} and e_g values began as soon as the results were obtained and put into spreadsheets. When looking at those area values, the only ones that should change across the

datasets are the t_{2g} areas while the e_g areas should be practically identical. This is because the t_{2g} orbital's occupancy will vary while the e_g orbital should not have any occupied states and return the same area value regardless of the compound. Because of this and the minimal impact of the arctangent on the t_{2g} 's Lorentzian component, the plots associated with that feature are of the greatest interest in looking for the correlation between area and d -orbital occupancy.

As is reflected below in table 1, the $4d$ row's L_3 -edge e_g area (labeled Area 2) appears to fluctuate around the twenty-nine range but there is a significant disparity for some of the compounds, which can also be seen in figure 19. The disparity in this value, which should be roughly the same through the whole row, is attributed to difficulty in knowing where to place the arctangent component of the function. Much the same is seen in table 2 for the L_2 -edge, with a visual display given in figure 20. As already mentioned, this difficulty will be described in far greater depth later, focusing on the values attributed to the Lorentzians for the moment. Returning to those values, the two parameters given little attention thus far are the widths and center points. With the Lorentzian equation being used in the fitting function, the width attributed to each peak tends to follow a particular pattern where the t_{2g} feature's width will be far more narrow than the e_g feature's. This disparity is observed in the lower occupancy compounds through the t_{2g} peak being taller than the e_g peak, which will cover more area as a shorter, broader feature. For the $4d$ row's L_3 -edge, the t_{2g} width values fall in a range from 1.46 eV to 2.33 eV while the e_g widths vary between 3.00 eV to 4.99 eV following the pattern described. The location of each Lorentzian's center may not strictly follow a pattern due to the specifics of each compound, but it does maintain an average difference of 3.3 eV for the L_3 -edge in this row. The t_{2g} trends for both L -edges are shown below in figures 17 and 18 with a trend line to aid in following the results.

Zr	d Occ.	Area 1	Area 2	Width 1	Width 2	Center 1	Center 2
BaZrO ₃	0	16.47	29.96	1.83	3.11	-3.46	0.01
Nb							
NbNd _{2-x} Ce _x Sr ₂ Cu ₂ O _{10-d}	0	14.90	30.19	1.66	3.92	-3.68	-0.08
Sr ₂ CrNbO ₆	0	15.47	36.90	1.95	5.08	-4.19	-0.15
Mo							
MoO ₃	0	16.24	29.99	1.93	3.66	-2.84	-0.07
Sr ₂ FeMoO ₆	1	11.53	29.45	2.33	4.11	-2.87	0.15
Ru							
Sr ₂ YRuO ₆	3	8.55	22.84	1.96	3.00	-3.12	0.09
La ₂ NiRuO ₆	4	4.21	30.45	1.46	3.66	-2.76	0.15
Rh							
La ₂ CuRhO ₆	5	0.00	29.15	0.00	4.00	NA	0.25
La ₂ Mn ₃ Rh ₄ O ₁₂	6	0.00	20.47	0.00	3.18	NA	0.25

Table 1: 4d L_3 -edge results as taken from Origin following application of curve fitting function.

Zr	d Occ.	Area 1	Area 2	Width 1	Width 2	Center 1	Center 2
BaZrO ₃	0	13.86	18.09	1.63	2.49	-3.30	0.05
Nb							
NbNd _{2-x} Ce _x Sr ₂ Cu ₂ O _{10-d}	0	13.40	19.31	1.50	3.63	-3.62	0.02
Sr ₂ CrNbO ₆	0	13.93	29.86	1.67	5.06	-4.06	-0.07
Mo							
MoO ₃	0	14.51	23.72	1.73	3.96	-2.63	0.19
Sr ₂ FeMoO ₆	1	14.05	23.75	2.27	4.01	-2.53	0.43
Ru							
Sr ₂ YRuO ₆	3	13.12	32.02	1.76	3.07	-2.88	0.02
La ₂ NiRuO ₆	4	2.58	34.68	1.21	2.85	-2.55	-0.11
Rh							
La ₂ CuRhO ₆	5	0.00	24.95	0.00	3.54	NA	0.19
La ₂ Mn ₃ Rh ₄ O ₁₂	6	0.00	21.11	0.00	3.21	NA	0.29

Table 2: 4d L_2 -edge results as taken from Origin following application of curve fitting function.

Figure 17: $4d$ L_3 -edge
 t_{2g} Area vs. Occupancy

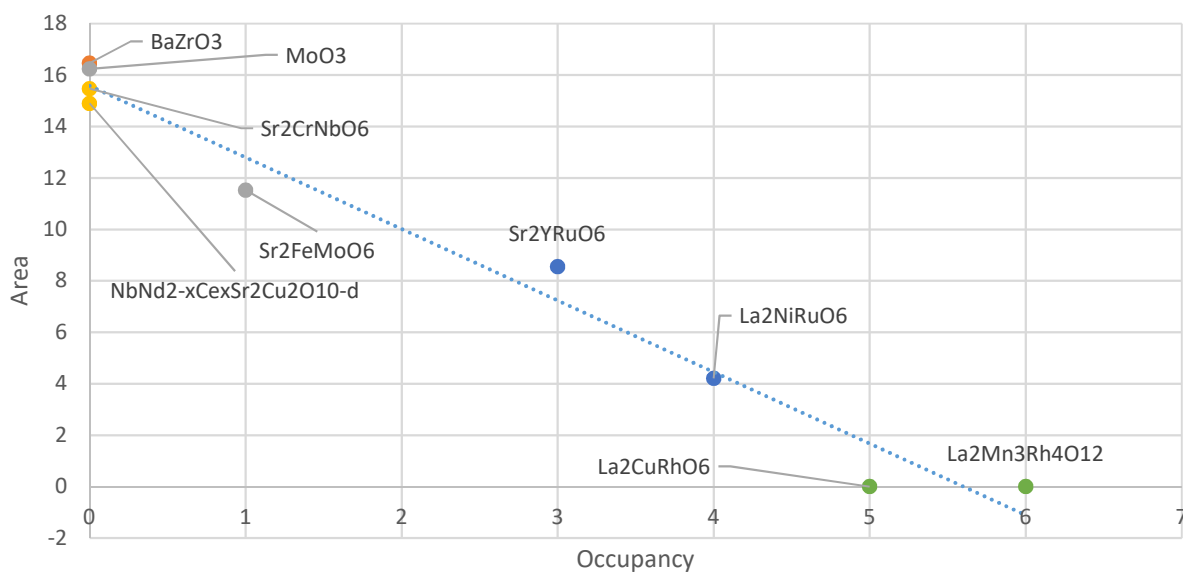
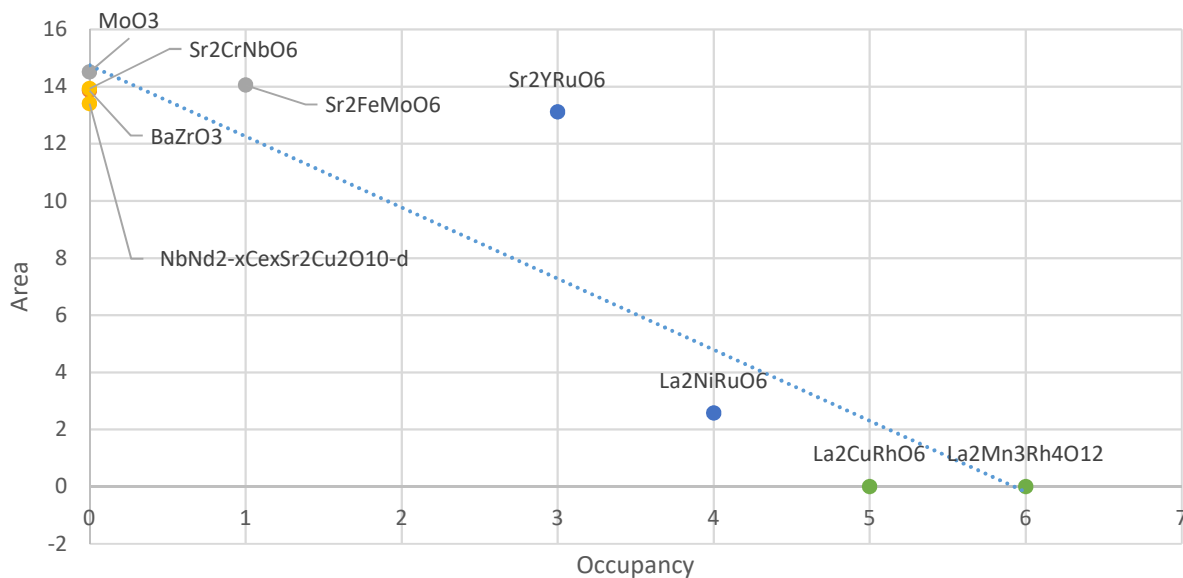


Figure 18: $4d$ L_2 -edge
 t_{2g} Area vs. Occupancy



Figures 17 & 18: Across both the L_3 - and L_2 -edges, a solid trend is shown for the $4d$ row in regards to t_{2g} area vs. d -orbital occupancy as expected, with one major outlier in the L_2 -edge with Sr_2YRuO_6 . These results show the potential for curve fitting XANES data.

Figure 19: $4d L_3$ -edge
 e_g Area vs. Occupancy

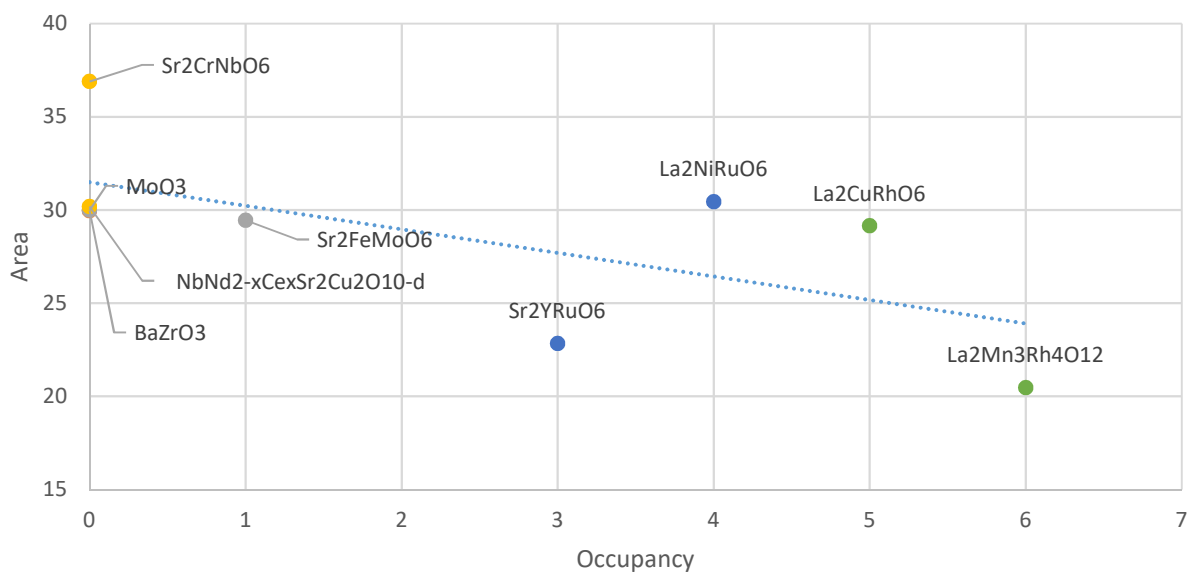
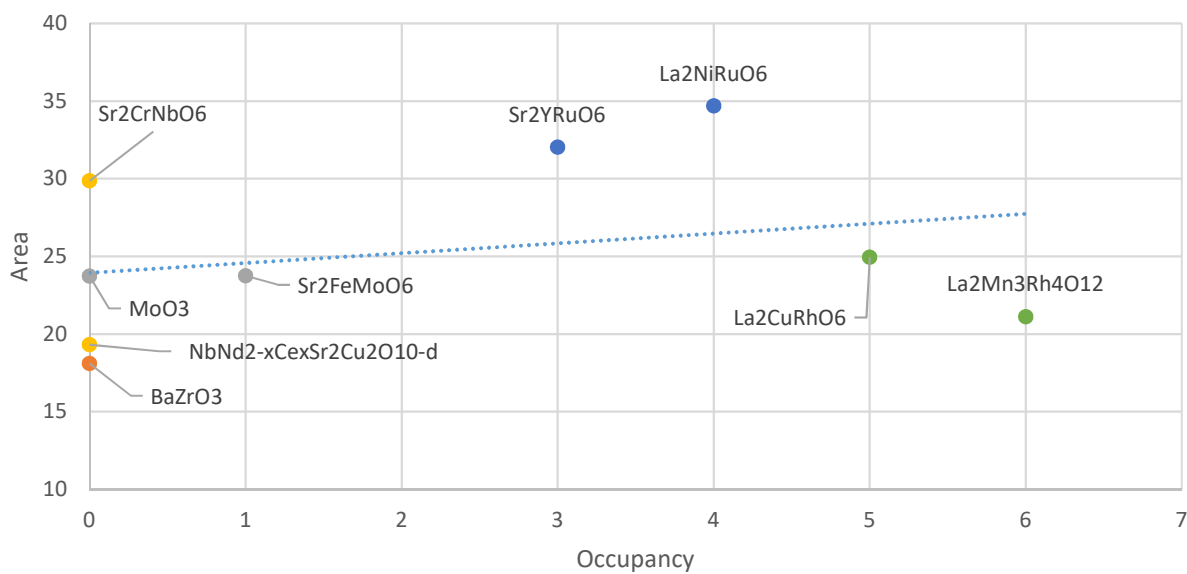


Figure 20: $4d L_2$ -edge
 e_g Area vs. Occupancy



Figures 19 & 20: The values for the e_g feature fluctuate more than desired but it is good to see that they seem centered around a particular range opening up the potential for pinning the values to obtain better future results.

With the $5d$ row, table 3 and 4 outline the Lorentzian values obtained by the curve fitting function in the L_3 -edge and L_2 -edge respectively. In every way, except for the far more consistent e_g values, the $5d$ row follows the patterns observed in the $4d$ row albeit with a slight, but noticeable, difference in scale. For instance, in table 3 the difference between the t_{2g} and e_g widths is more pronounced with the t_{2g} peaks falling between 4.19 eV and 5.67 eV compared to the e_g widths of 6.69 eV to 8.33 eV. Much the same is the case for the center point differences in this edge for the $5d$ row with the average value being 4.2 eV between the two peaks. All in all, the results coming out of the $5d$ row provides a satisfying picture of what is going on for each compound, most importantly following along the d -orbital occupancy trends that are to be expected as a proof of concept, which are shown in figures 21 through 24.

<i>Ta</i>	d Occ.	Area 1	Area 2	Width 1	Width 2	Center 1	Center 2
$\text{Ca}_2\text{MnTaO}_6$	0	14.91	29.70	5.06	8.18	-3.95	0.88
<i>W</i>							
Sr_2MnWO_6	0	16.36	31.21	5.12	8.18	-4.48	0.70
<i>Re</i>							
$\text{Sr}_4\text{Fe}_3\text{ReO}_{12}$	0	16.35	31.67	5.03	7.99	-4.12	0.58
$\text{Mn}_2\text{CoReO}_6$	1	12.27	29.25	4.95	7.87	-3.41	0.98
$\text{Ba}_2\text{MnReO}_6$	1	11.58	32.68	4.62	7.75	-3.67	0.57
$\text{Sr}_2\text{MnReO}_6$	1	11.51	30.47	4.62	6.96	-3.43	0.49
$\text{Pb}_2\text{CrReO}_6$	2	12.27	27.45	5.67	8.33	-2.09	1.61
$\text{Mn}_2\text{FeReO}_6$	2	11.30	30.71	5.63	8.27	-3.50	0.68
<i>Ir</i>							
$\text{Sr}_2\text{CaIrO}_6$	3	5.66	34.69	4.30	8.33	-3.67	0.06
$\text{Sr}_2\text{ScIrO}_6$	4	4.57	34.01	4.19	8.15	-2.99	0.37
$\text{La}_2\text{CuIrO}_6$	5	0.00	35.37	0.00	8.06	NA	0.18

Table 3: $5d$ L_3 -edge results showing area, width, and center point values for both the t_{2g} and e_g peaks respectively.

<i>Re</i>	d Occ.	Area 1	Area 2	Width 1	Width 2	Center 1	Center 2
Sr ₄ Fe ₃ ReO ₁₂	0	23.43	24.43	5.21	8.16	-4.58	-0.01
Mn ₂ CoReO ₆	1	14.79	26.63	4.75	7.92	-4.07	0.38
Pb ₂ CoReO ₆	1	14.15	26.67	5.31	8.64	-4.40	-0.27
Ba ₂ MnReO ₆	1	13.74	29.77	4.41	8.30	-3.37	0.86
Pb ₂ CrReO ₆	2	13.49	25.33	5.34	8.45	-1.87	1.70
<i>Ir</i>							
Pb ₂ CrIrO ₆	2	13.27	25.12	5.25	8.44	-1.22	2.36
Sr ₂ CaIrO ₆	3	4.15	25.58	4.30	8.75	-3.21	0.34
Sr ₂ ScIrO ₆	4	0.00	21.89	0.00	7.26	NA	0.32
La ₂ CuIrO ₆	5	0.00	21.24	0.00	7.66	NA	0.10

Table 4: $5d$ L_2 -edge results showing area, width, and center point values for both the t_{2g} and e_g peaks respectively.

Figure 21: $5d$ L_3 -edge
 t_{2g} Area vs. Occupancy

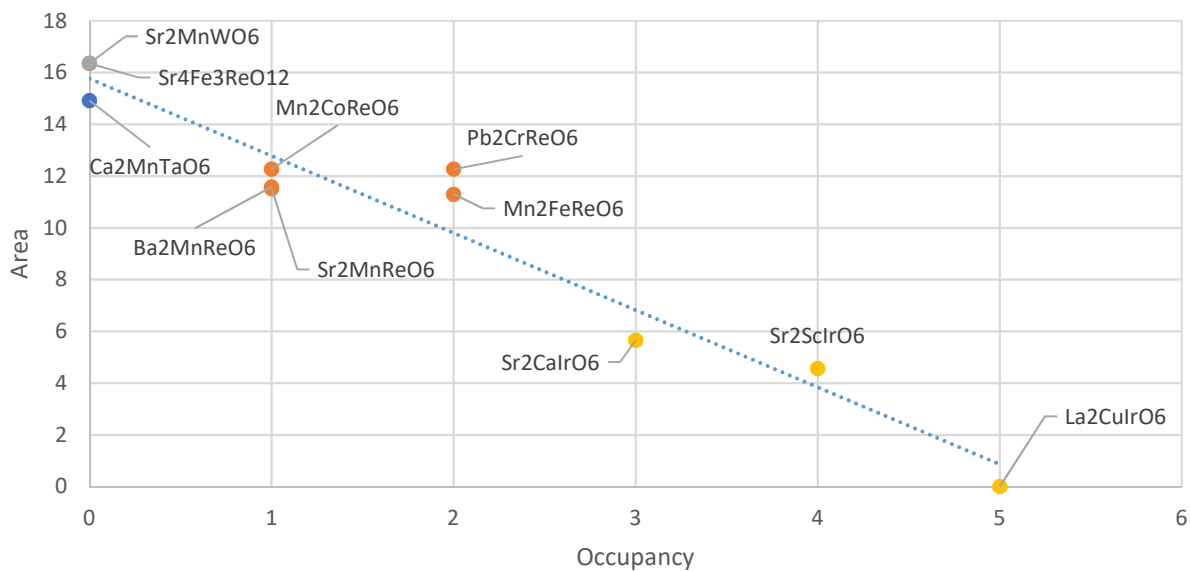
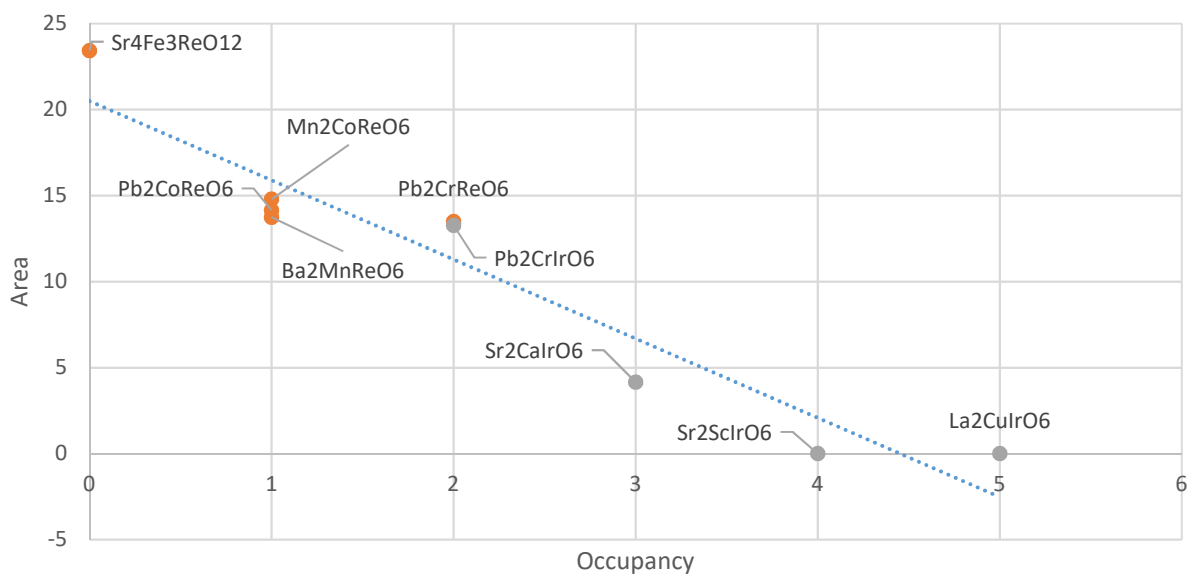


Figure 22: $5d$ L_2 -edge
 t_{2g} Area vs. Occupancy



Figures 21 & 22: the $5d$ row t_{2g} trend is far stronger than for the $4d$ row with fantastic grouping based on d -orbital occupancy.

Figure 23: L_3 -edge
 e_g Area vs. Occupancy

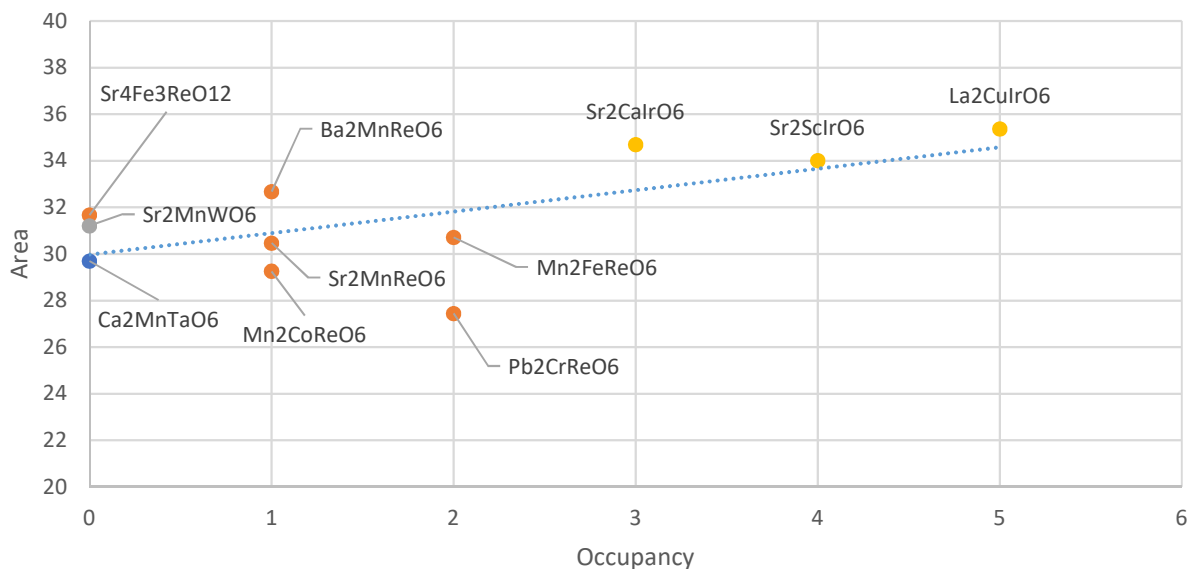
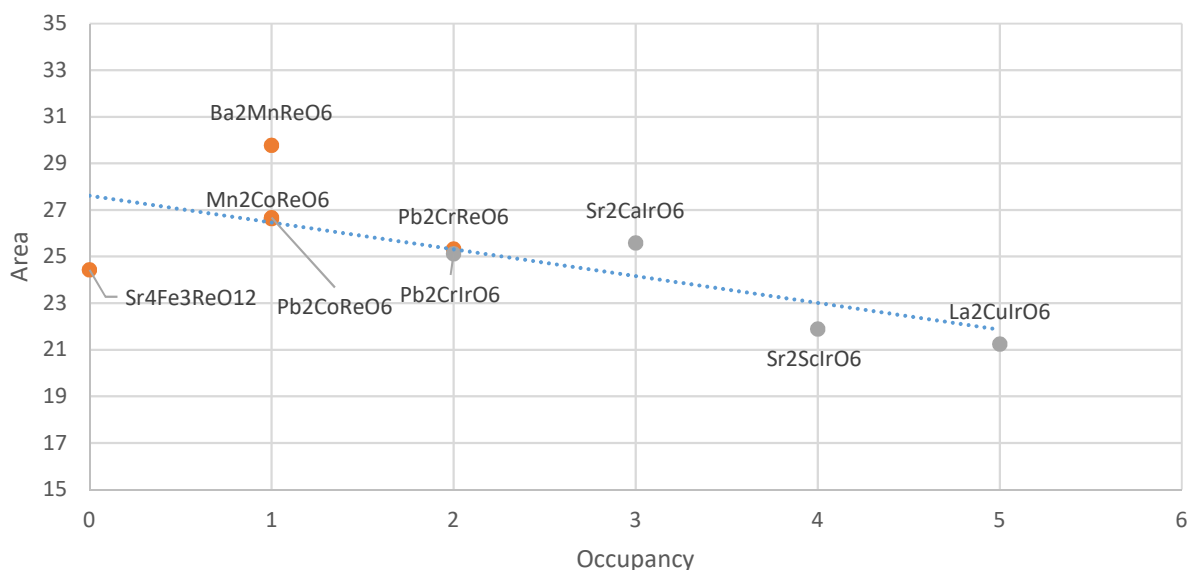


Figure 24: 5d L_2 -edge
e_g Area vs. Occupancy



Figures 23 & 24: the e_g plots for the 5d row $L_{2,3}$ -edges are more tightly grouped than for the 4d row but there is still room for improvement as the trend should be a flat line.

These values have all been compiled in the search of any interesting patterns inherit to each row and provide further backing to what trends exist in connection with the d -orbital occupancy of a TMO. This information was also of great use when going through the later stages of curve fitting in order to have a general idea on the points necessary for the fitting function to track different samples in each row. By this I mean that, rather than having to split up the peaks in each edge, it was possible to use a general set of guiding values for the fitting function thus streamlining the technique. Although this information is useful, it is important to note that the areas are the only ones correlated with d -orbital occupancy in a blatant manner. So, there is significant utility in having the full variable set for each compound as it simplifies applying the technique to any TMO seeking to be tested in a similar way.

Having discussed the t_{2g} and e_g components of the $L_{2,3}$ -edges, the plots to dissect next are for the area sums versus d -orbital occupancy. These are of interest because the plots produced will show which compounds in particular need further refinement as far as the curve fitting is concerned. It is certainly possible that the fluctuations that are seen in figures 22 and 23 for the $4d$ row have to do with the XANES data itself because there are more matrix element effects and other potential problem spots present compared to the $5d$ row. Keeping this in mind as well as the inconsistency of the e_g values seen previously, the area sum plots still provide an adequate, if shaky, showing for the correlation between area and d -orbital occupancy.

Figure 25: $4d$ L_3 -edge
Area Sum vs. Occupancy

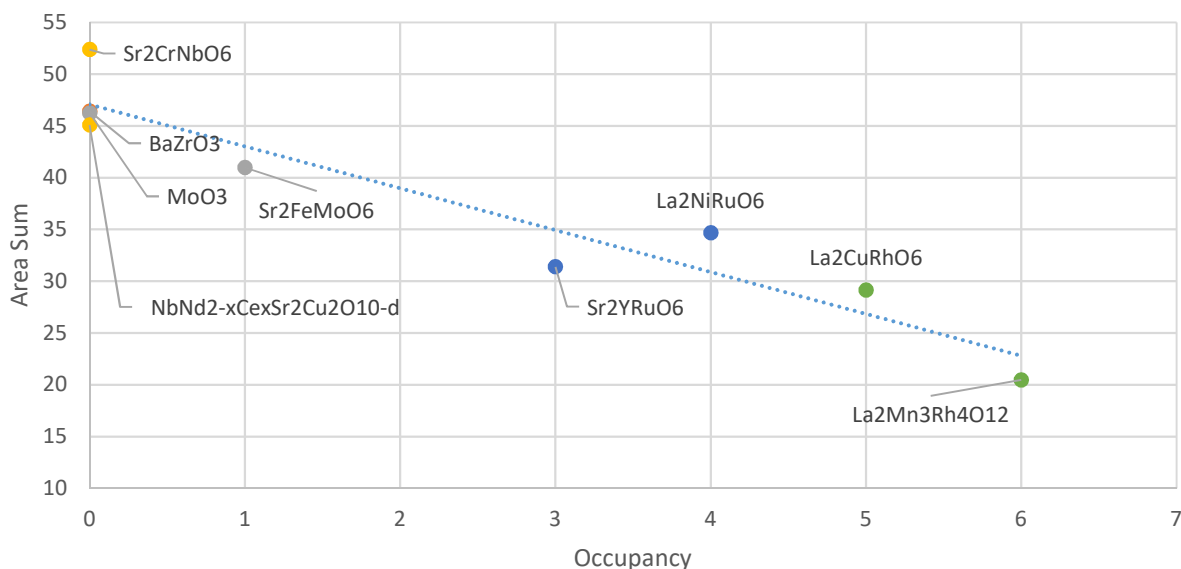


Figure 26: $4d$ L_2 -edge
Area Sum vs. Occupancy

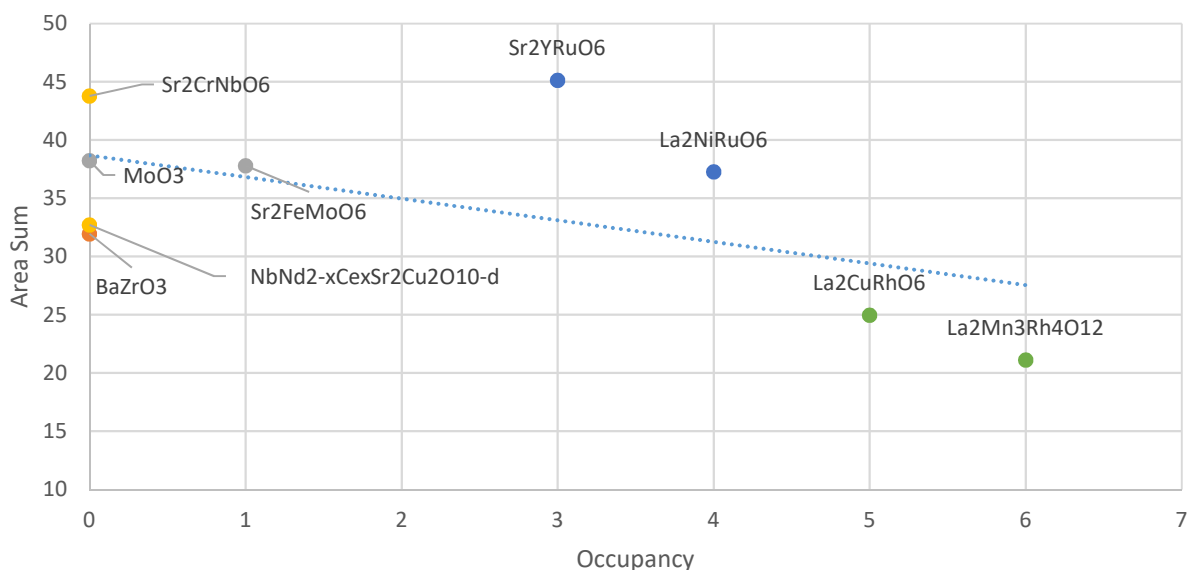
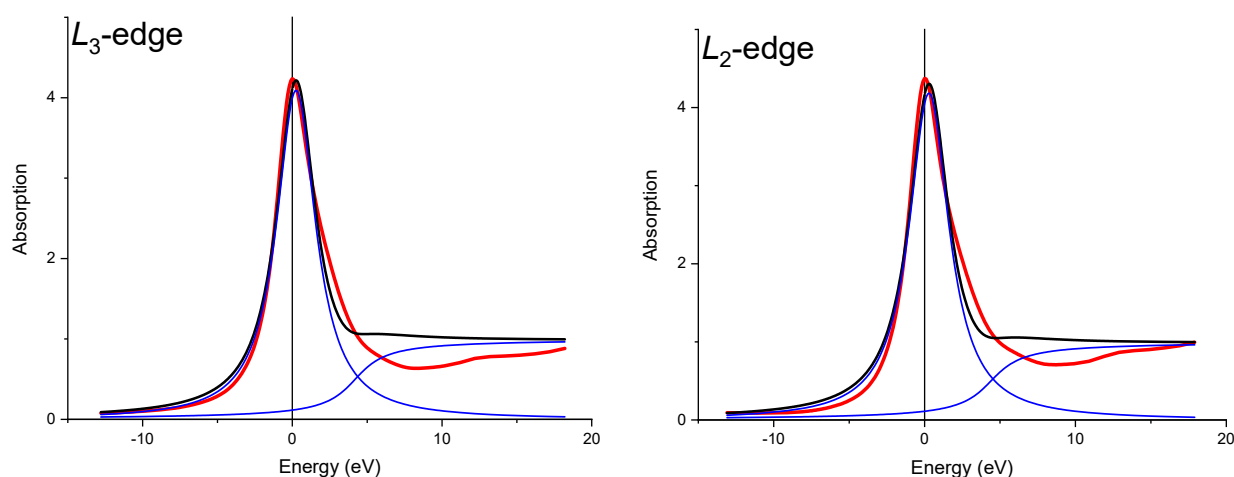


Figure 25 & 26: L_3 -edge area sum vs. d -orbital occupancy (top) and L_2 -edge area sum vs. d -orbital occupancy (bottom) for the $4d$ row begin to show the decreasing trend that is expected as the number of open states in the d -orbital decreases.

Despite the outliers, there is a trend being followed for the total area in figures 25 and 26 across both the L_2 - and L_3 -edges with the L_3 -edge following the best. Looking back to the t_{2g} and e_g values, those outliers become more understandable especially when considering the continuum's contribution. For some of the outliers, it will be shown when looking at examples of their fits that being able clearly tell where the error is coming from although I suspect a significant portion comes from placing the arctangent's inflection point and this can be seen in figures 27 and 28.



Figures 27 & 28: $\text{La}_2\text{Mn}_3\text{Rh}_4\text{O}_{12}$'s L_3 -edge (Left) and L_2 -edge (Right) show the difficulty in fitting when the t_{2g} is nonexistent along with the complexity of placing the arctangent component. (Images from Origin 2019b)

With the $5d$ row, the results are far more impressive when looking at the area sums in figures 29 and 30 as well. Considering the t_{2g} , e_g splitting was far less pronounced than in the $4d$ row it was somewhat surprising to get. Once again, the compounds that had mostly filled t_{2g} orbitals had a degree of complexity in attempting to fit them. It appears to me that, when fitting the white-line features, there is a degree of “tilting” that should be noticeable in the fit images that is not covered well when the t_{2g} feature drops away. Returning to the $5d$ row results as a whole, there is an incredibly clear trend that is closely followed by the compounds in regards to their total areas and area ratios.

Figure 29: $5d$ L_3 -edge
Area Sum vs. Occupancy

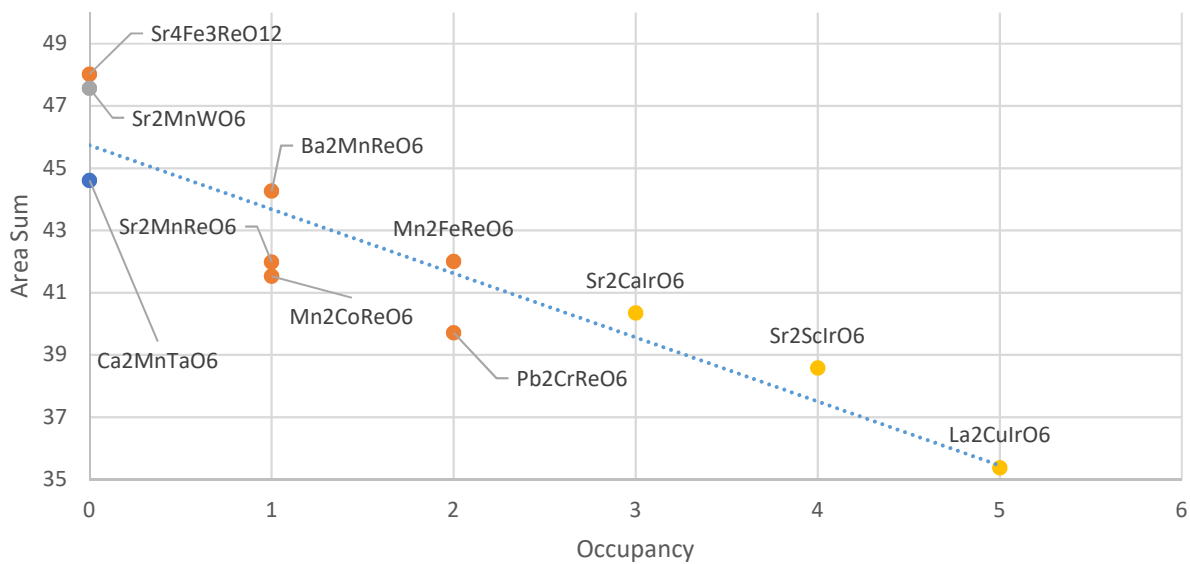
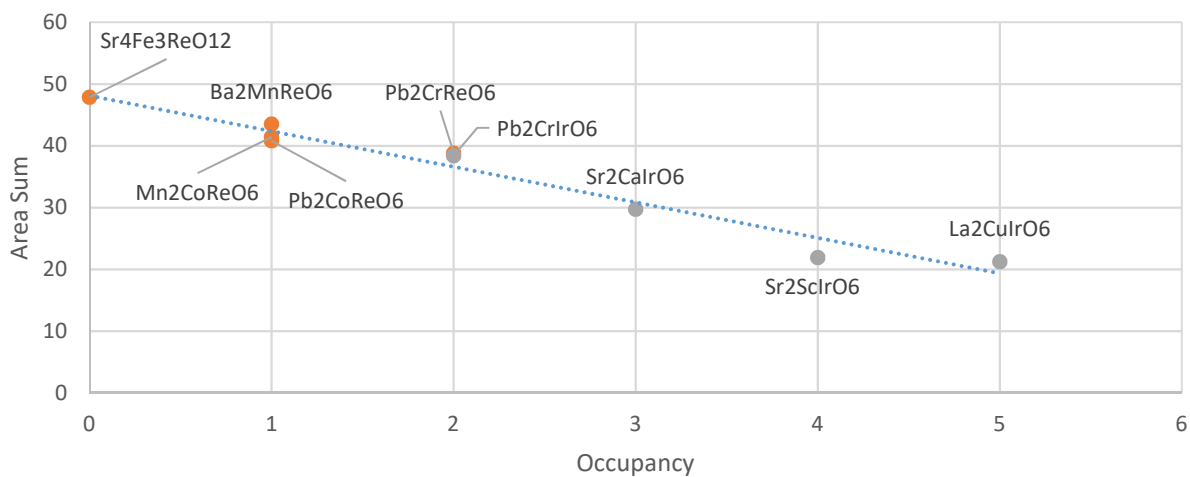


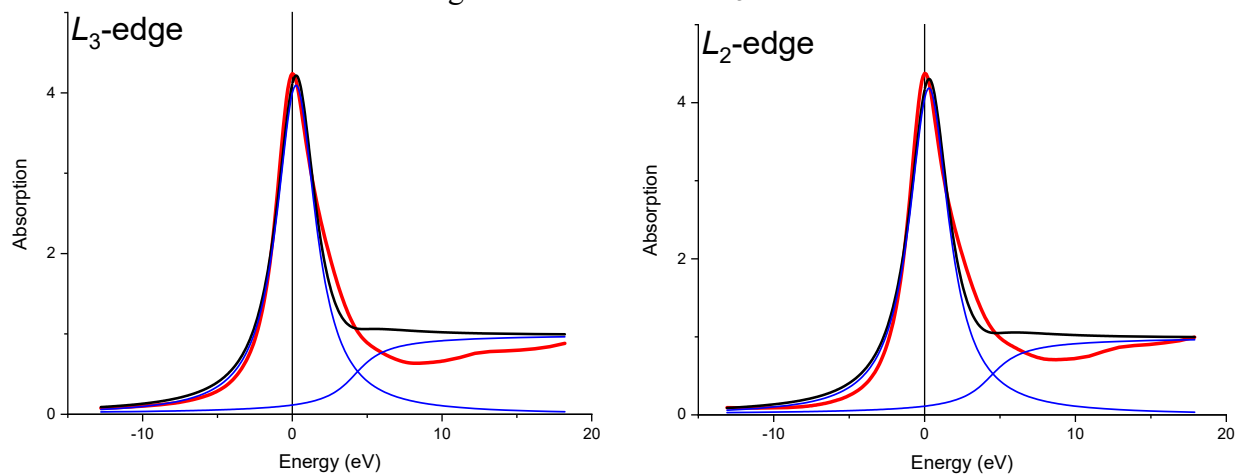
Figure 30: $5d$ L_2 -edge
Area Sum vs. Occupancy



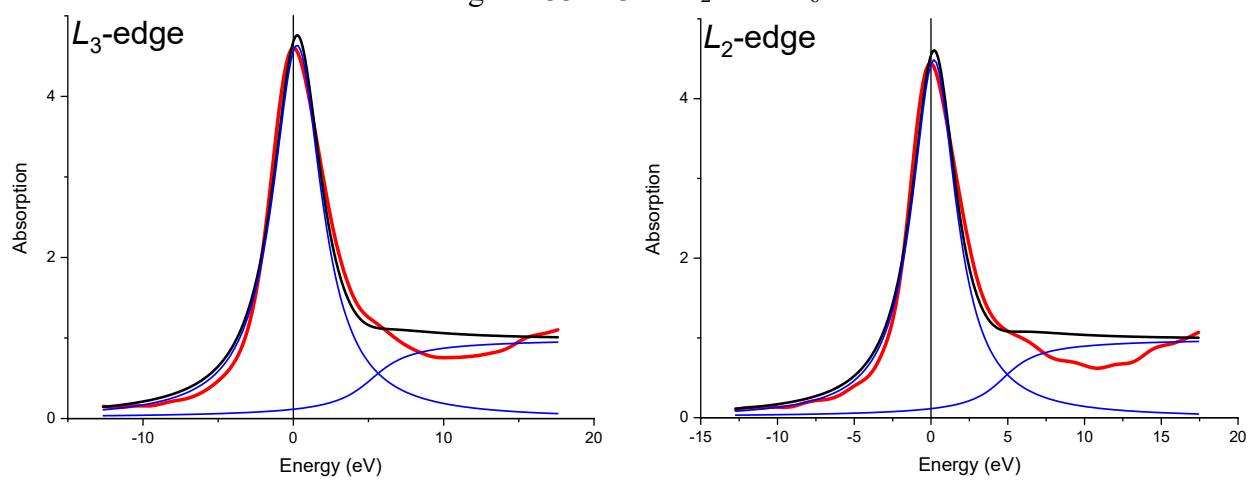
Figures 29 & 30: L_3 -edge area sum vs. d -orbital occupancy (top) and L_2 -edge area sum vs. d -orbital occupancy (bottom) for the $5d$ row adequately show the decreasing trend that is expected as the number of open states in the d -orbital decreases.

Selection of Curve Fits (4d Row): (The following images are from Origin 2019b)

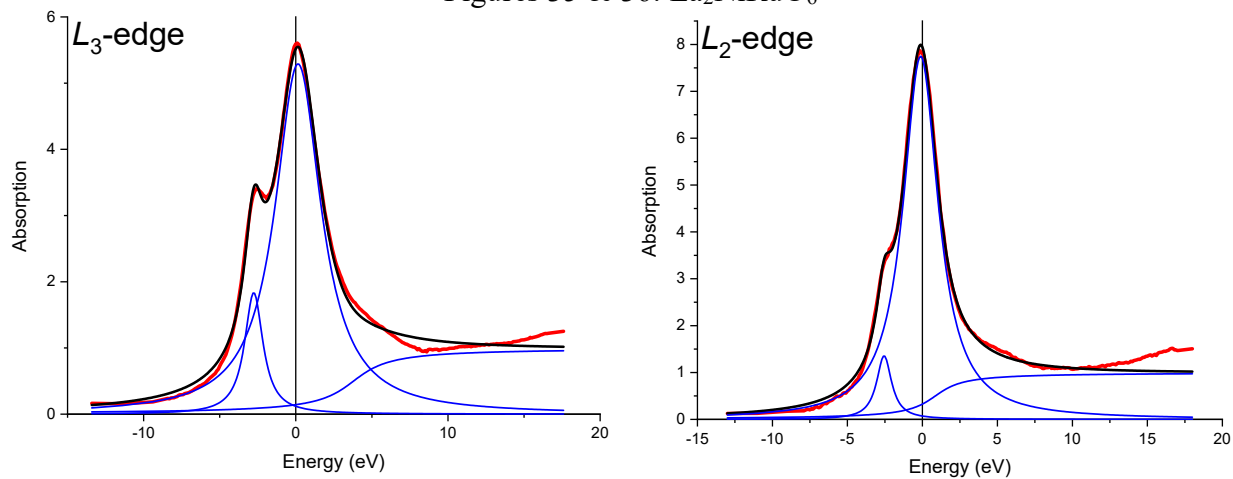
Figures 31 & 32: $\text{La}_2\text{Mn}_3\text{Rh}_4\text{O}_{12}$



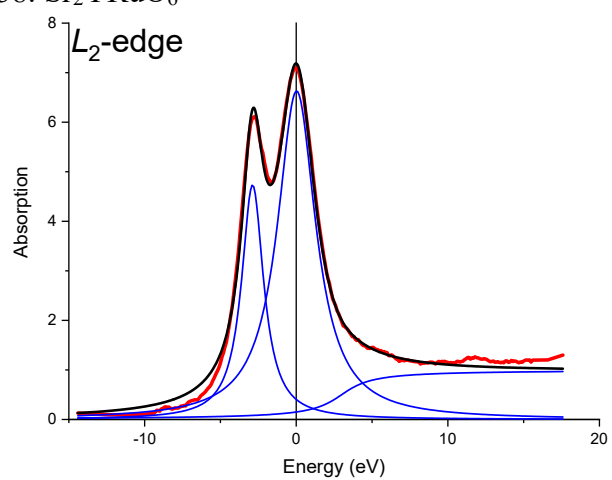
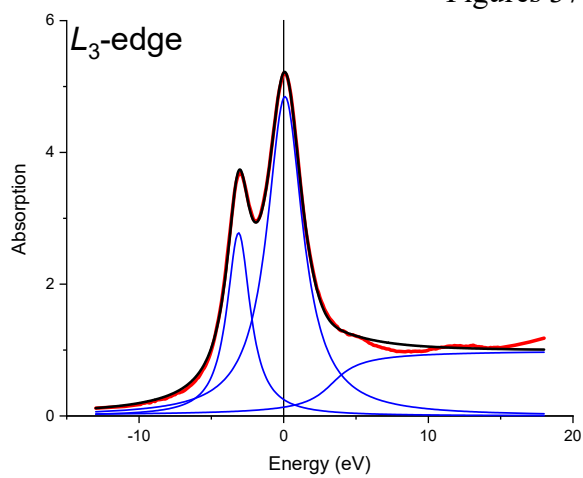
Figures 33 & 34: $\text{La}_2\text{CuRhO}_6$



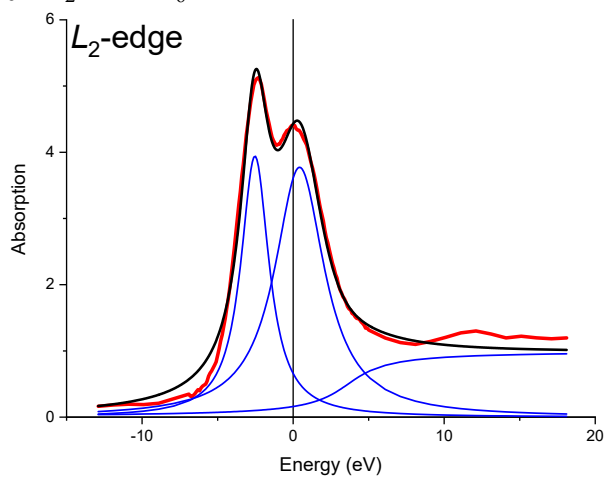
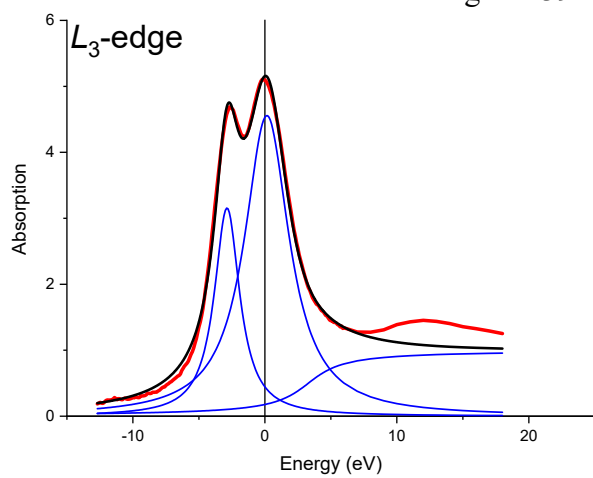
Figures 35 & 36: $\text{La}_2\text{NiRuO}_6$



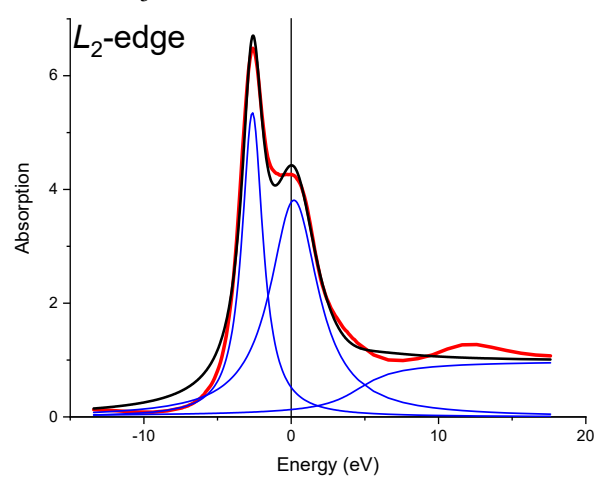
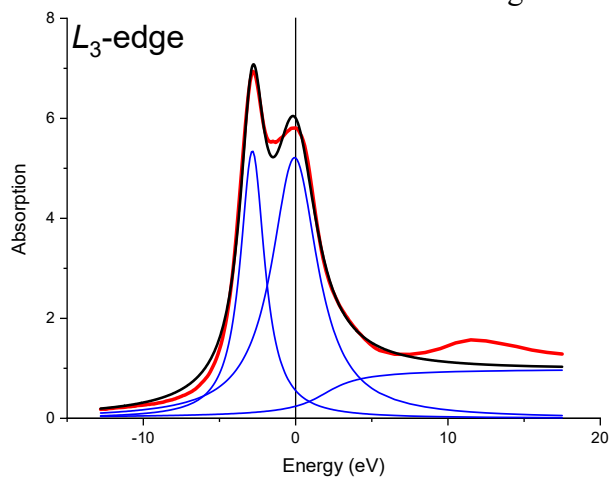
Figures 37 & 38: Sr_2YRuO_6



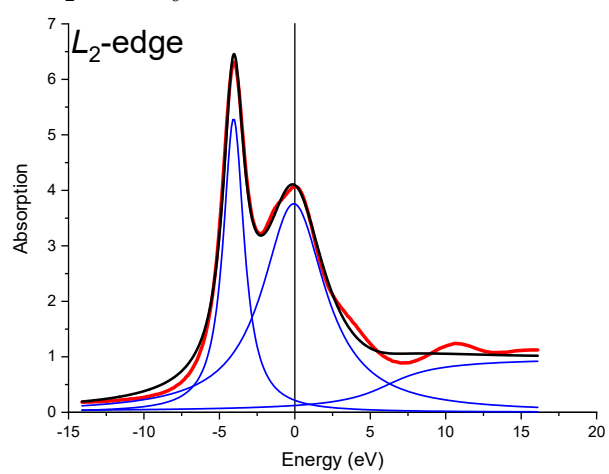
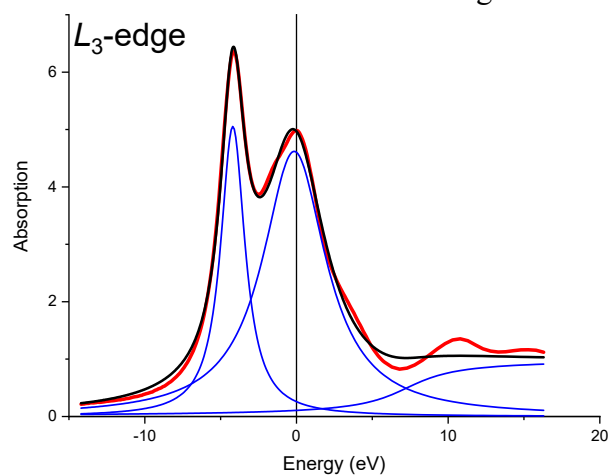
Figures 39 & 40: $\text{Sr}_2\text{FeMoO}_6$



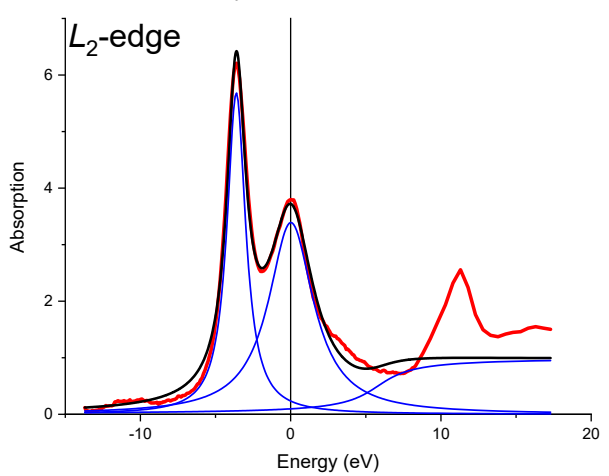
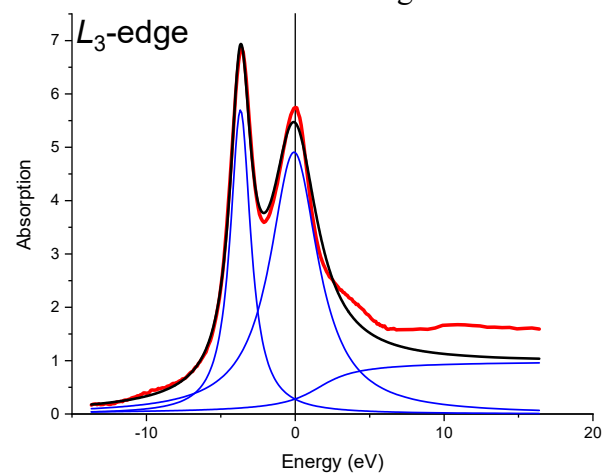
Figures 41 & 42: MoO_3



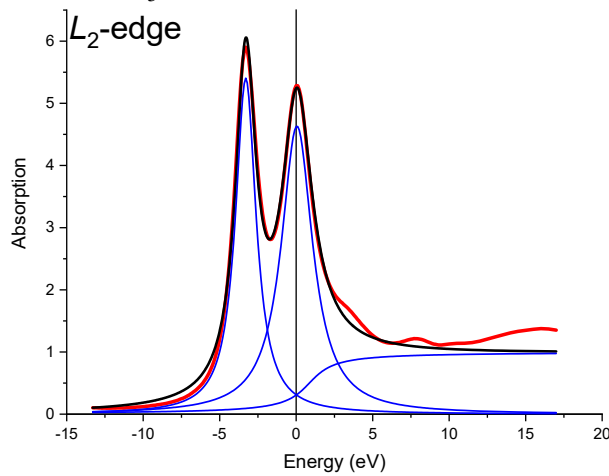
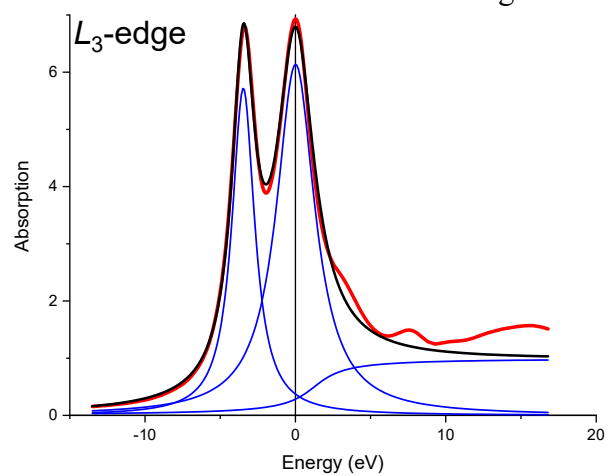
Figures 43 & 44: $\text{Sr}_2\text{CrNbO}_6$



Figures 45 & 46: $\text{NbNd}_{2-x}\text{Ce}_x\text{Sr}_2\text{Cu}_2\text{O}_{10-d}$

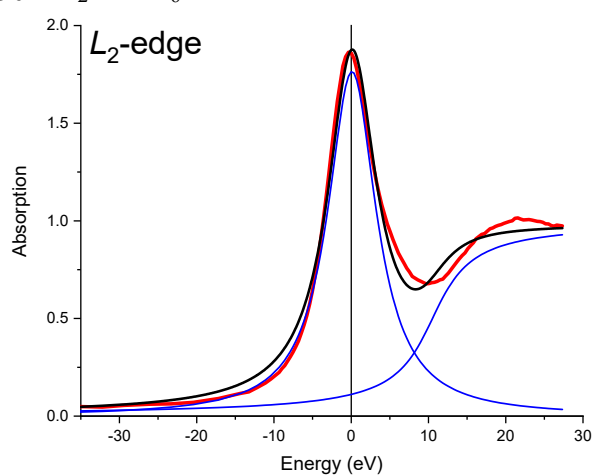
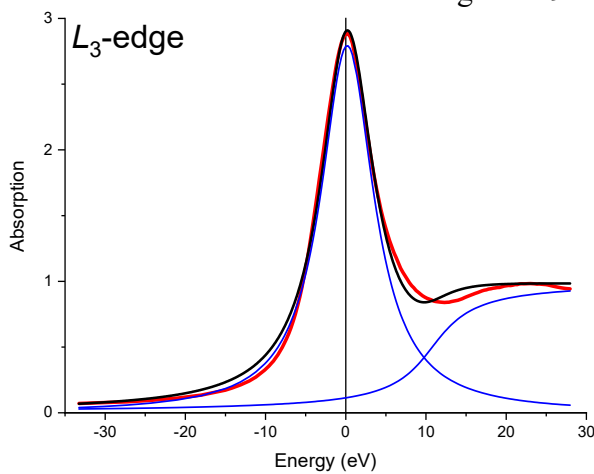


Figures 47 & 48: BaZrO_3

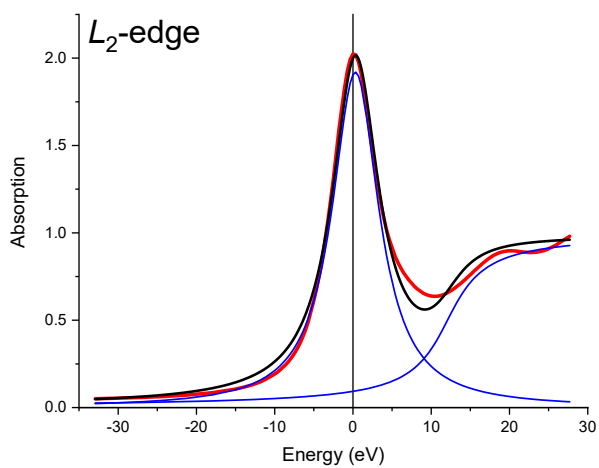
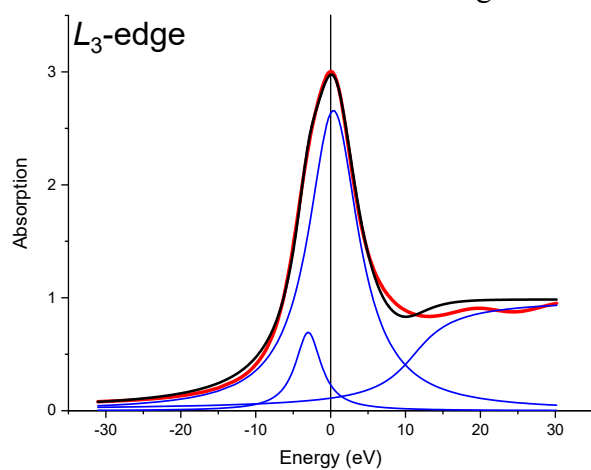


Selection of Curve Fits (5d Row): (The following images are from Origin 2019b)

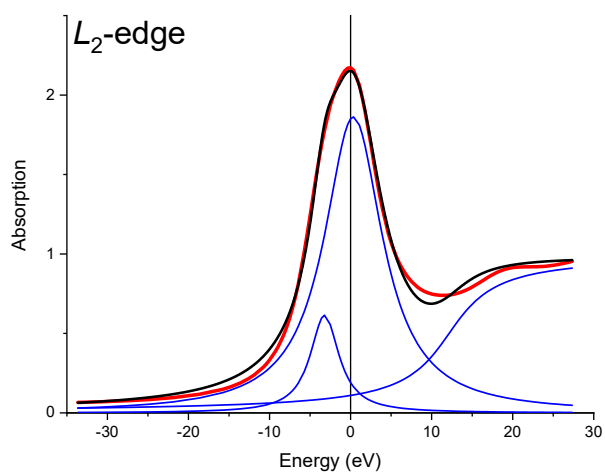
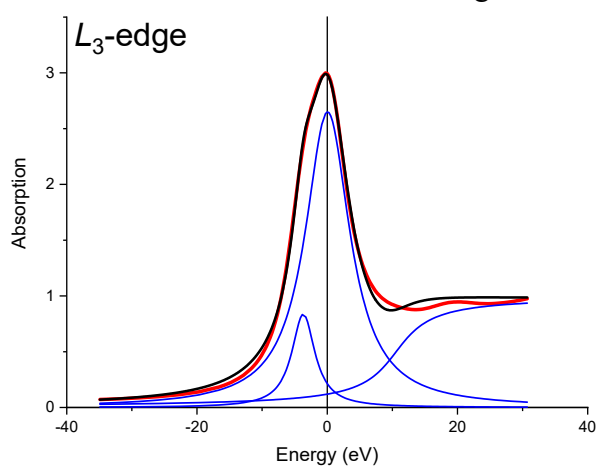
Figures 49 & 50: $\text{La}_2\text{CuIrO}_6$



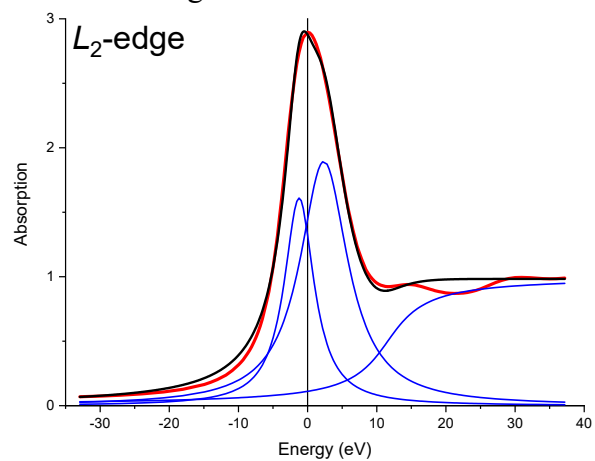
Figures 51 & 52: $\text{Sr}_2\text{ScIrO}_6$



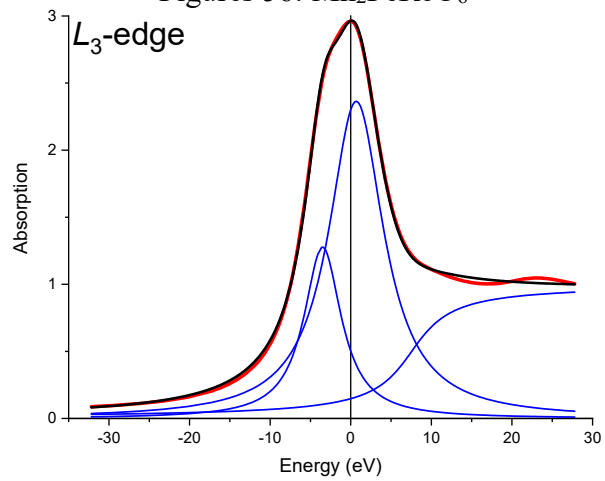
Figures 53 & 54: $\text{Sr}_2\text{CaIrO}_6$



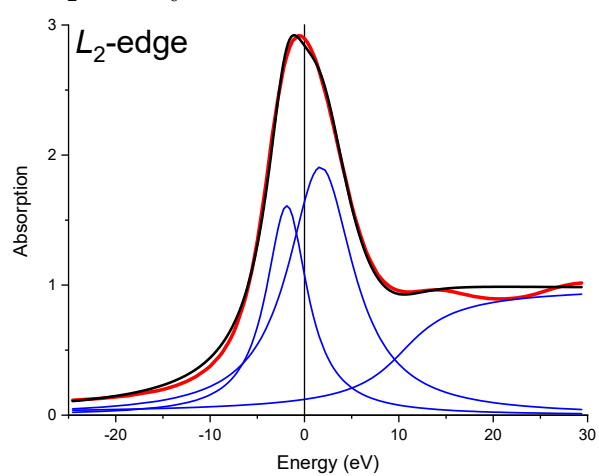
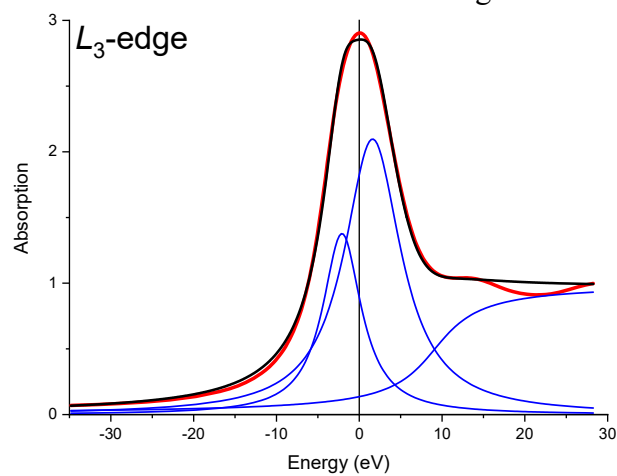
Figures 55: $\text{Pb}_2\text{CrIrO}_6$



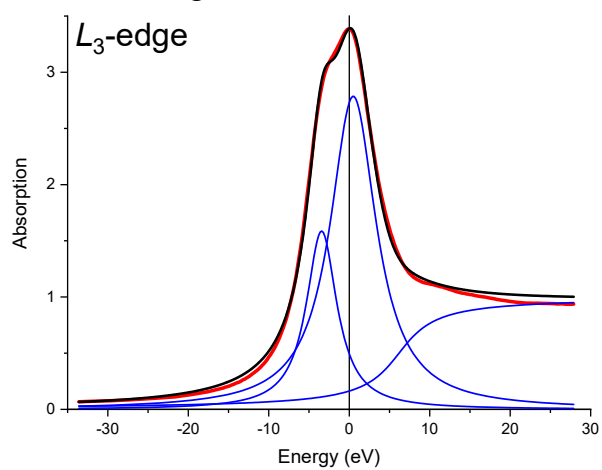
Figures 56: $\text{Mn}_2\text{FeReO}_6$



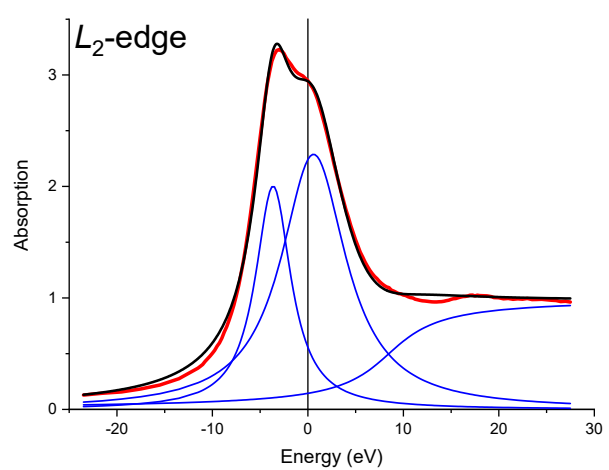
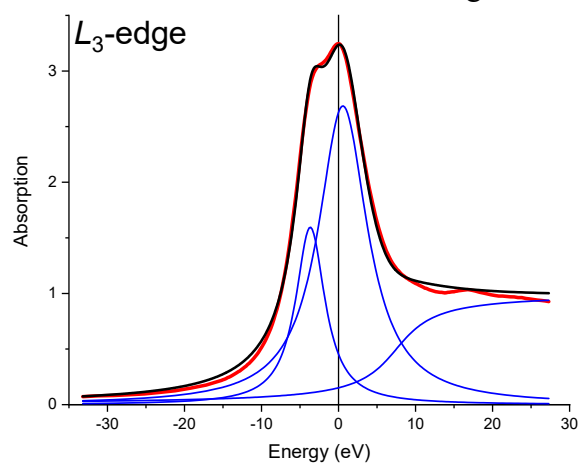
Figures 57 & 58: $\text{Pb}_2\text{CrReO}_6$



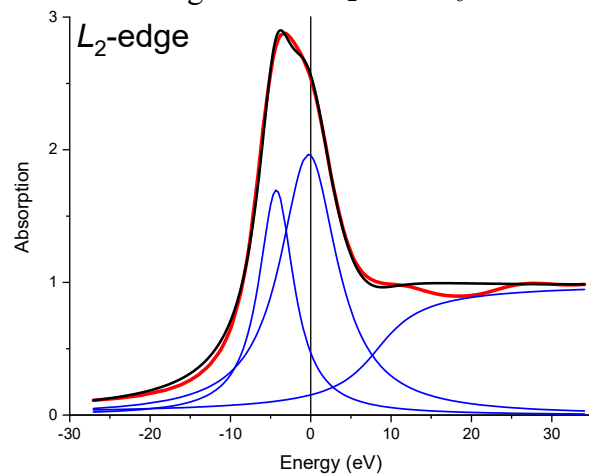
Figures 59: $\text{Sr}_2\text{MnReO}_6$



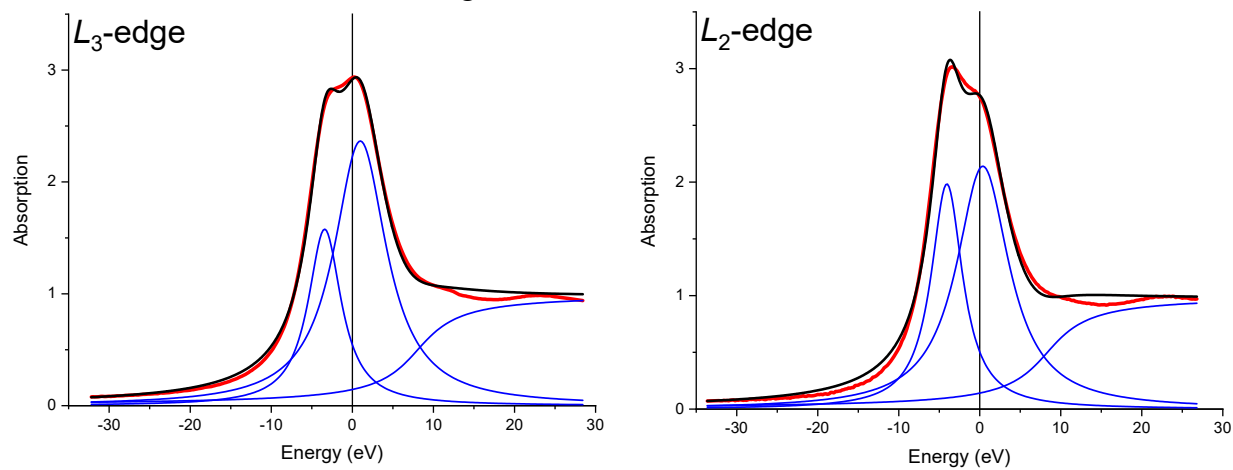
Figures 60 & 61: $\text{Ba}_2\text{MnReO}_6$



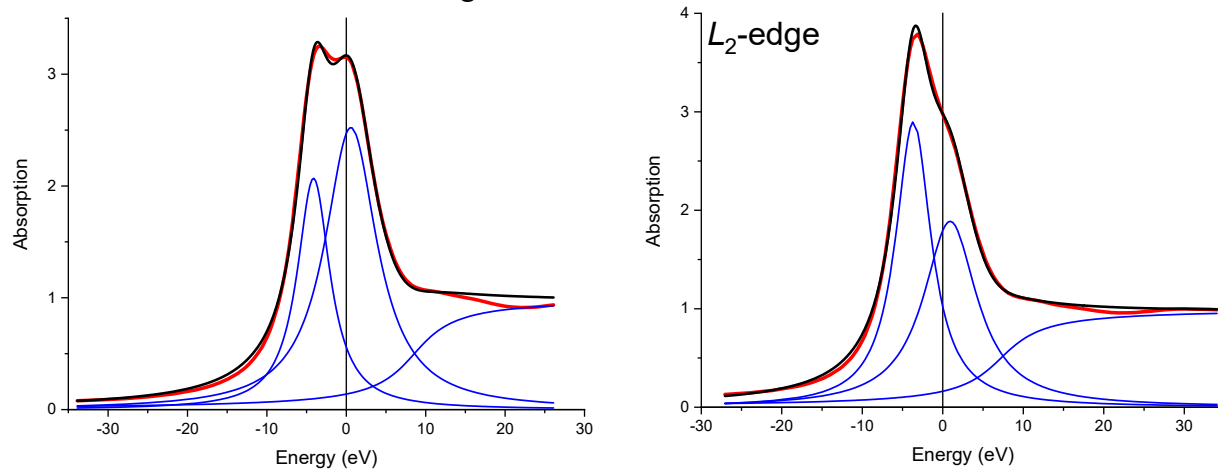
Figures 62: $\text{Pb}_2\text{CoReO}_6$



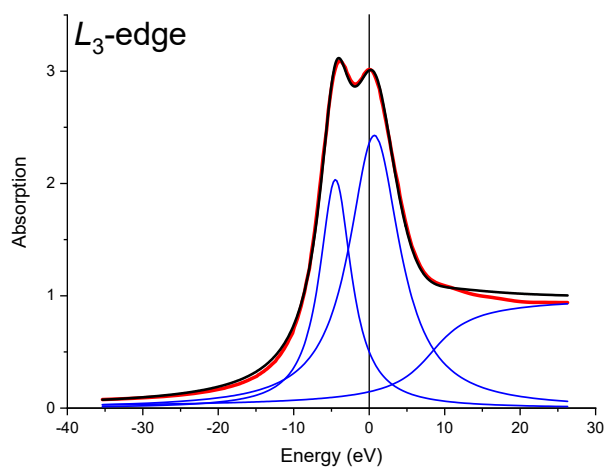
Figures 63 & 64: $\text{Mn}_2\text{CoReO}_6$



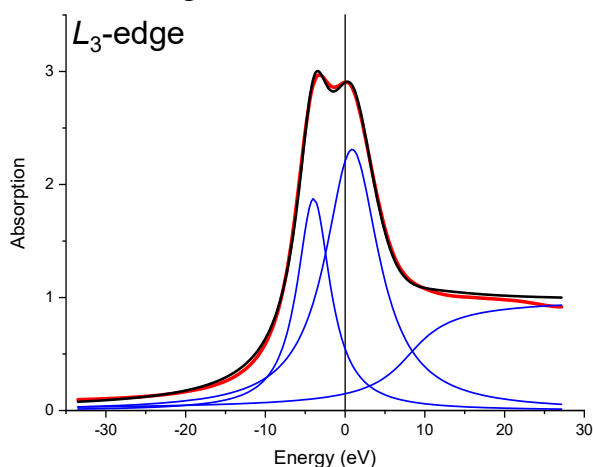
Figures 65 & 66: $\text{Sr}_4\text{Fe}_3\text{ReO}_{12}$



Figures 67: Sr_2MnWO_6



Figures 68: $\text{Ca}_2\text{MnTaO}_6$



The Arctangent Continuum:

As should be easily noticed across figures 31 through 68 and has already been briefly discussed, the arctangent component leads to a great deal of complexity. Simply put, the arctangent could be located over a significant range underneath the white-line feature. This is a massive problem that has to be dealt with. In order to make some headway, the continuum has been defined so that it does not come before the e_g feature. The continuum also should not be directly be located directly underneath that e_g feature; it should instead come a fair distance past the feature while not being vastly beyond it. The new problem becomes how to determine where in that, still sizable energy range, the arctangent component should be located. Of course, the specific location will change depending on the spectra of different compounds but it should follow some general trend across a row.

With the $4d$ row, there was a significant amount of uncertainty surrounding the arctangent component of the fitting function, which is reflected in Table 3. This uncertainty was warranted when looking at the results, particularly the e_g area plots shown previously because that is the feature that will be most severely affected by where the arctangent's inflection point is

located as it will cut into the Lorentzian if located too close to the peak. When attempting to correct for this it was necessary, however, to not go too far in pushing the arctangent past the peak since the continuum is meant to directly follow each edge. So for this row it is difficult to say for certain where the inflection point is located, although with more time it can likely be pinned down.

Zr	Center 2	ArcTan Height	X-Int	ArcTan Width
BaZrO ₃	0.01	1/ π	1.26	1.55
Nb				
NbNd _{2-x} Ce _x Sr ₂ Cu ₂ O _{10-d}	-0.08	1/ π	1.59	1.96
Sr ₂ CrNbO ₆	-0.15	1/ π	7.29	2.54
Mo				
MoO ₃	-0.07	1/ π	1.93	1.83
Sr ₂ Cr _{1.2} Mo _{0.8} O ₆	0.52	1/ π	7.00	2.49
Sr ₂ FeMoO ₆	0.15	1/ π	3.30	2.06
Sm ₂ Mo ₂ O ₇	0.10	1/ π	6.68	2.39
Ru				
Sr ₂ YRuO ₆	0.09	1/ π	3.38	1.50
La ₂ NiRuO ₆	0.15	1/ π	3.80	1.83
Rh				
La ₂ CuRhO ₆	0.25	1/ π	5.25	2.00
La ₂ Mn ₃ Rh ₄ O ₁₂	0.25	1/ π	4.20	1.59

Table 3: $4d$ L_3 -edge arctangent results. Center of e_g feature also shown for comparison to arctangent inflection point.

Switching over to the $5d$ row, the previously mentioned and displayed trends are due, largely in part, to being able to more easily place the continuum. This comparative simplicity is likely due to the larger energy range over which the $5d$ row TMOs WL features cover. That is to say that for a comparable analysis to be conducted between the $4d$ and $5d$ rows, the $5d$ row's peaks will cover close to twice the energy range. This larger energy range seemed to more completely unlock the fitting function's capability to resolve and place the continuum. It may also simply be the case that in the $5d$ row, the continuum is better resolved providing the cleaner

results. This row also ends up having a well displayed trend which becomes apparent when comparing the central point of the e_g feature to the inflection point of the arctangent continuum which is reflected in Table 4. Regardless, the cooperation of the arctangent for this subset of TMOs goes to show how effective the fitting technique can be.

<i>Ta</i>	Center 2	ArcTan Height	X-Int	ArcTan Width
$\text{Ca}_2\text{MnTaO}_6$	0.88	$1/\pi$	8.11	4.09
<i>W</i>				
Sr_2MnWO_6	0.70	$1/\pi$	8.32	4.09
<i>Re</i>				
$\text{Sr}_4\text{Fe}_3\text{ReO}_{12}$	0.58	$1/\pi$	8.52	3.99
$\text{Mn}_2\text{CoReO}_6$	0.98	$1/\pi$	8.07	3.94
$\text{Ba}_2\text{MnReO}_6$	0.57	$1/\pi$	7.51	3.87
$\text{Sr}_2\text{MnReO}_6$	0.49	$1/\pi$	6.18	3.48
$\text{Pb}_2\text{CrReO}_6$	1.61	$1/\pi$	9.14	4.17
$\text{Mn}_2\text{FeReO}_6$	0.68	$1/\pi$	7.56	4.13
<i>Ir</i>				
$\text{Sr}_2\text{CaIrO}_6$	0.06	$1/\pi$	10.59	4.17
$\text{Sr}_2\text{ScIrO}_6$	0.37	$1/\pi$	11.17	4.07
$\text{La}_2\text{CuIrO}_6$	0.18	$1/\pi$	10.79	4.03

Table 4: $5d$ L_3 -edge arctangent results. There does appear to be a trend when comparing the e_g feature's center to the inflection point of the arctangent.

ERROR ANALYSIS

The $4d$ row is problematic when looking at the values that are collected across the XANES data set. Particularly when observing the disparity that appears in the e_g area values, it is evident that the fitting process needs further refinement. In Origin, the e_g areas have averaged standard errors of 0.90 and 0.79 for the L_3 - and L_2 -edges respectively. The t_{2g} areas comparatively have averaged standard errors of 0.36 and 0.41 respectively. The t_{2g} error being lower than for e_g is unsurprising considering the t_{2g} values will be less severely impacted by the arctangent component of the fitting function but they can prove difficult to resolve when the only indication to their existence is a small “shoulder” in the XANES spectra.

In the $5d$ row, a similar difference between the e_g and t_{2g} areas’ standard errors as outlined in Origin is present. Compared to the $4d$ row, the standard errors attributed to the $5d$ row are larger. As could be seen in the plots and figures, however, the values themselves are in better agreement with one another. For the e_g areas, the averaged standard errors are 1.22 and 1.53 for the L_3 - and L_2 -edges respectively and 1.01 and 1.55 for the t_{2g} areas. For both rows, the error associated with the L_3 -edge is lower than for the L_2 -edge, which is likely due to the less intense WL features present in the L_2 -edge. The lower intensity lends itself to increased difficulty in separating the t_{2g} , e_g , and continuum components.

The arctangent itself is difficult to quantitatively determine the error for because it is not well enough understood how it should be set up in regards to the inflection point and its width. To simplify the situation, the width was defined by the e_g Lorentzian’s half-width but this is serving to cut back on the number of floating variables. There is the potential that in every case, much like for the height, the width should be fixed to a particular value, which would likely vary by row.

CONCLUSION

The non-linear least squares curve fitting technique displayed here provides substantial proof that such a method could be put to great use in future XANES research. It is able to obtain the systematics of the L_2 - and L_3 -edge white-line features with a fair degree of accuracy, particularly for the $5d$ row. There are improvements that need to be made in regards to the $4d$ row breakdown that are directly tied to locating the inflection point of the continuum. Upon such an improvement in the technique, the full potential will be unlocked. Until then, the t_{2g} feature values can be taken with more weight as they are less influenced by the continuum's effects. The t_{2g} features adequately follow the expected d -orbital occupancy trend and should be looked to more highly than the area sum plots. There is still much to learn from the information that can be obtained through curve fitting XANES data.

As for the efficiency of the technique, being able to take normalized XANES data, window it to a useable size, and then drop it into a program such as Origin made for comparatively easy to obtain results. The time factor is also considerable as going from windowed XANES data to results takes only moments so long as the guiding parameters for the fitting function are reasonable for whatever program is being used to follow. That being said, when fitting across a broad collection of XANES $L_{2,3}$ data, it is possible to determine the trend that will be followed when it comes to the guiding parameters making the process far simpler. If the continuum has a definite trend, defining it by that trend in the fitting function will further increase the efficacy of this technique. In the event that the trend is row dependent as I suspect, a tweaked formula could be introduced accordingly.

The results collected have been shown to be encouraging across both rows but particularly the $5d$ row. The sources of error can be simplified down to a determination of how

capable the Lorentzian distribution is at tracking the WL features and the significant complexity in pinpointing the arctangent's parameters, specifically the width and inflection point. The Lorentzian is effective at capturing the “simpler” cases where there is no asymmetry in the feature being fit but for the samples where the lead in is sharper than the trailing edge, the Lorentzian becomes less effective. Based on my own observations, the arctangent is the most significant source of error. It is undoubtedly capable of skewing the area values for the e_g features when placed incorrectly. During early tests with the fitting function, changes in the width of the arctangent will directly alter the widths that the function attributes to the Lorentzians showing how significant the continuum is to accurately fitting XANES data.

When looking to analyze the results obtained from this technique, it is best executed when there are samples to compare to. The results on their own, with nothing to compare to, do not currently hold significant value. It is when they are placed alongside the results for other compounds that the systematics yield important information. I am curious if it would be possible to establish standard acceptable ranges for the areas to fall under per d -orbital occupancy to simplify future testing and the determination of unknowns. In comparing across the $4d$ and $5d$ rows, good pictures are drawn outlining the trends in occupancy in each row and with the previously mentioned refinement, such compilations will benefit future studies into the $L_{2,3}$ -edges of transition metal oxides.

REFERENCES

1. G. Cao and L. De-Long, *Frontiers of 4d- and 5d-Transition Metal Oxides*. (2013).
2. B. Qi, I. I. Perez, P. H. Ansari, F. Lu and M. Croft, *Phys Rev B Condens Matter* **36** (5), 2972-2975 (1987).
3. L. W. Martin, Y. H. Chu and R. Ramesh, *Materials Science and Engineering: R: Reports* **68** (4-6), 89-133 (2010).
4. J. Chen, M. Croft, Y. Jeon, X. Xu, S. A. Shaheen and P. Ansari, *Solid State Communications* **85**, 291-296 (1993).
5. Y. Jeon, B. Qi, F. Lu and M. Croft, *Phys Rev B Condens Matter* **40** (3), 1538-1545 (1989).
6. G. Liang, A. Sahiner, M. Croft, W. Xu, X. Xiang, D. Badresingh, W. Li, J. Chen, J. Peng, A. Zettl and F. Lu, *Phys Rev B Condens Matter* **47** (2), 1029-1035 (1993).
7. G. Popov, M. Greenblatt and M. Croft, *Physical Review B* **67** (2) (2003).
8. M. W. Ruckman, G. Reisfeld., Najeh M. Jisrawi, M. Weinert and M. Strongin, *Phys Rev B Condens Matter* **57** (7), 3881-3886 (1998).
9. Y. H. Cheng, J. C. Jan, J. W. Chiou, W. F. Pong, M. H. Tsai, H. H. Hseih, Y. K. Chang, T. E. Dann, F. Z. Chien, P. K. Tseng, M. S. Leu and T. S. Chin, *Applied Physics Letters* **77** (1), 115-117 (2000).
10. Y. Jeon, J. Chen and M. Croft, *Phys Rev B Condens Matter* **50** (10), 6555-6563 (1994).
11. J. A. Horsley, *The Journal of Chemical Physics* **76** (3), 1451-1458 (1982).
12. D. C. Koningsberger and R. Prins, *X-Ray Absorption: Principles, Applications, Techniques of EXAFS, SEXAFS and XANES*, 1 ed. (Wiley-Interscience, 1988).

13. J. A. Van Bokhoven and C. Lamberti, *X-Ray Absorption and X-Ray Emission Spectroscopy*. (2016).
14. P. Duke, *Synchrotron Radiation: Production and Properties*. (Oxford University Press, USA, 2009).
15. G. Bunker, *Introduction to XAFS*, 1 ed. (Cambridge University Press, 2010).